2017-05-01

Multipath Channel Considerations in Aeronautical Telemetry

Edem Coffie Gagakuma
Brigham Young University

Multipath Channel Considerations in Aeronautical Telemetry

Edem Coffie Gagakuma

A thesis submitted to the faculty of
Brigham Young University
in partial fulfillment of the requirements for the degree of

Master of Science

Michael Rice, Chair
Brian D. Jeffs
David G. Long

Department of Electrical and Computer Engineering

Brigham Young University

ABSTRACT

Multipath Channel Considerations in Aeronautical Telemetry

Edem Coffie Gagakuma
Department of Electrical and Computer Engineering, BYU
Master of Science

This thesis describes the use of scattering functions to characterize time-varying multipath radio channels. Channel Impulse responses were measured at Edwards Air Force Base (EAFB) and scattering functions generated from the impulse response data. From the scattering functions we compute the corresponding Doppler power spectrum and multipath intensity profile. These functions completely characterize the signal delay and the time varying nature of the channel in question and are used by systems engineers to design reliable communications links. We observe from our results that flight paths with ample reflectors exhibit significant multipath events.

We also examine the bit error rate (BER) performance of a reduced-complexity equalizer for a truncated version of the pulse amplitude modulation (PAM) representation of SOQPSK-TG in a multipath channel. Since this reduced-complexity equalizer is based on the maximum likelihood (ML) principle, we expect it to perform optimally than any of the filter-based equalizers used in estimating received SOQPSK-TG symbols. As such we present a comparison between this ML detector and a minimum mean square error (MMSE) equalizer for the same example channel. The example channel used was motivated by the statistical channel characterizations described in this thesis. Our analysis shows that the ML equalizer outperforms the MMSE equalizer in estimating received SOQPSK-TG symbols.

Keywords: scattering function, multipath, maximum likelihood equalizer, minimum mean square error equalizer

ACKNOWLEDGMENTS

The research published in this thesis is the result from collaborating with at least half a dozen students. I'm grateful for their involvement and friendship. To name a few: Christopher Hogstrom, Christopher Nash, Keith Thompson, and Colt Thomas.

I'm also grateful for other current and past students who offered friendship and advice on both personal and technical issues. Notably: Andrew McMurdie, Grant Wagner, Jonathan Spencer, Richard Black, Benjamin Arnold, James Eck, and Jeff Ravert.

I'm grateful for the BYU Electrical Engineering faculty who have instructed me, given me counsel and treated me like a peer. It's been so fun developing friendships that extended outside of campus, especially having lunches with my faculty adviser, friend and mentor Michael Rice. Dr. Rice's leadership style has helped me grow as a person and his light-hearted demeanor made learning a delight.

My biggest cheerleader has been my godfather Henry Nyarko. I'm ever grateful for his relentless confidence in me.

TABLE OF CONTENTS

LIST OF TABLES

LIST OF FIGURES

NOMENCLATURE

$h(\tau; t)$	Complex-valued impusle response
t	Variable representing time
τ	Variable representing delay
$\phi_k(t)$	Variable representing path phase
$R_h(\tau, \Delta t)$	Autocorrelation of a wide-sense stationary uncorrelated scattering (WSSUS) channel
$S(\tau; \lambda)$	Scattering function
λ	Doppler frequency
$S(\lambda)$	Doppler Power Spectrum
$s(\Delta t)$	Spaced-time correlation function
$\rho(\tau)$	Multipath intensity profile
$R(\Delta f)$	Spaced-frequency correlation function
Δf	Frequency separation
$\bar{\tau}$	Mean excess delay
σ_τ	RMS delay spread
$\mathbf{M}$	Notation for matrices (bold upper case letters)
$\mathbf{v}$	Notation for vectors (bold lower case letters)
I	Transmitted symbol
$\hat{I}$	Estimate of transmitted symbol at the output of receiver
$p(t)$	Pulse shaping filter
h_c	Low-pass equivalent impulse response of a mutlipath channel
$e(k)$	Equalizer output error

Subscripts, superscripts, other indicators and abbreviations

$\mathbf{M}^{-1}$	indicates the inverse of a square matrix $\mathbf{M}$
$[\,]^\dagger$	indicates Hermitian or conjugate transpose of $[\,]$
$[\,](t)$	indicates $[\,]$ is a function of time, in the t domain
$[\,](\tau)$	indicates $[\,]$ is a function of delay, in the τ domain
$[\,]_0$	indicates $[\,]$ is evaluated at time t or τ equal to zero
$[\,]_p$	indicates $[\,]$ is referenced by the index p
SOQPSK-TG	represents shaped offset quadrature phase shift keying- telemetry group version
EAFB	represents Edwards Air Force Base
AGC	represents automatic gain control
LHCP	represents left-hand-circular polarization
RHCP	represents right-hand-circular polarization
BER	represents bit error rate
Pt.	represents Point
NAS	represents Naval Air Station
EHF	represents extremely high frequency
WSSUS	represents wide-sense stationary uncorrelated scattering
AWGN	represents additive white Gaussian noise
PAM	represents pulse amplitude modulation
ML	represents maximum likelihood
MMSE	represents minimum mean square error

CHAPTER 1. INTRODUCTION

1.1 Motivation

Multipath interference is one of the dominant channel impairments in aeronautical telemetry. This multipath phenomenon is mostly attributed to objects that scatter or diffract propagating waves. Time variations occurring in the channel are usually caused by mobile transmitters and receivers coupled with changes in the wireless medium itself.

Significant effort over the past 10 years has characterized multipath fading at L- and S-bands for low, and medium-altitude flights over desert ranges like EAFB, California and at EHF-band for low- and medium-altitude flights over the ocean at Pt. Mugu NAS. The mathematical models derived from these experiments have been published in [2], [3] and [4] and are used in software simulations by government laboratories, industry development laboratories, and in academic research efforts. In addition, mathematical models from these publications have been used to configure hardware for bench testing in most government laboratories. This observation points to the primary benefit of producing an accurate channel model. Channel models allow new transmission and/or receiver methods to be tested in software simulation. This permits the identification of promising candidates for improving telemetry without the need for expensive and lengthy hardware developments. A secondary, but important benefit is a fundamental understanding of the multipath propagation mechanisms. This has the potential to plan "smart" flight profiles. For example, it might be possible to schedule critical tests when the airborne transmitter is in a location that is not susceptible to mutlipath interference.

Statistically characterizing time varying multipath channels is often accomplished using the scattering function. This function helps us understand two things:

- how fast the channel is changing; and
- channel power as a function of multipath delay.

We make two fundamental assumptions before proceeding with the mathematical formulation required for deriving scattering functions using multipath channel impulse responses:

1. The multipath channel may be correctly modeled as a wide-sense stationary (WSS) random process.

2. The scattering (multipath delays) are statistically uncorrelated.

In general, the first assumption is observably untrue. But perhaps over a sufficiently short temporal window, this assumption is approximately true. The second assumption is also untrue. But we will temporarily forget that we know this and see what the results give us. We will be cautious in drawing any firm conclusions in the final analysis, but some general trends can be observed in our results.

We follow our statistical characterization of multipath channels with an analysis of multipath mitigation techniques. We derive the maximum likelihood (ML) equalizer for SOQPSK-TG over a simple channel motivated by the statistical characterizations. The complexity of the ML detector is reduced using a truncated version of the pulse amplitude modulation (PAM) representation for SOQPSK-TG. SOQPSK-TG is examined because it is the most popular modulation defined in the standard for aeronautical telemetry, IRIG 106 [5]. As part of our analysis of the bit error rate performance (BER) of the ML equalizer for the simple channel, we generate the BER performance for an MMSE equalizer using SOQPSK-TG over the channel for which the ML equalizer was designed. Our results show that for the example channel used in our simulations, the reduced-complexity ML equalizer operates on a 64-state trellis and outperforms the MMSE equalizer by a wide margin.

This thesis is structured as follows: we outline a process for characterizing multipath channels by generating scattering functions for impulse response data collected during channel sounding experiments at Edwards Air Force Base (EAFB), California. Motivated by the channel characterizations, we present an example multipath channel for which we derive the ML equalizer using a truncated version of the PAM approximation of SOQPSK-TG. We generate the BER performance for the ML equalizer, and also generate the BER performance for the same example channel using the MMSE equalizer so we can compare the ML BER performance with the MMSE BER performance. Our analysis provides wireless communications engineers with added tools to understand

multipath phenomena and also, design detectors that mitigate against channel distortions caused by multipath propagation.

CHAPTER 2. CHARACTERIZING MULTIPATH PROPAGATION

2.1 Statistical Behavior of Linear-Time-Variant Channels

The material from this section is adapted from Hashemi [6] and Chapter 13 of Proakis and Salehi [2]. The traditional method for modeling multipath propagation in a mobile wireless communication system is to employ a linear-time-variant system. The linear-time-variant model is represented by the complex-valued low pass equivalent of a real-valued bandpass channel impulse response $h(\tau; t)$. This impulse response is two-dimensional and for L propagation paths, is given by

$$h(\tau; t) = \sum_{k=0}^{L-1} a_k(t)\delta(\tau - \tau_k(t))e^{j\theta_k(t)}, \tag{2.1}$$

where τ and t are the delay and time variables, respectively. One fixes the time variable t at $t = t_0$ and observes the impulse response $h(\tau; t_0)$. For the scenario looked at, this model characterizes a set of path arrival times $\tau_k(t)$, path amplitudes $a_k(t)$, and path phases $\theta_k(t)$. With the channel impulse response $h(\tau; t)$, we are ready to compute the autocorrelation function. We define the autocorrelation function as

$$R_h(\tau_1, \tau_2; t_1, t_2) = E\{h(\tau_1; t_1)h^*(\tau_2; t_2)\}. \tag{2.2}$$

Because $h(\tau; t)$ is assumed to be WSS, the autocorrelation can be written as

$$R_h(\tau_1, \tau_2; \Delta t) = E\{h(\tau_1; t)h^*(\tau_2; t + \Delta t)\}, \tag{2.3}$$

where $\Delta t = t_1 - t_2$. Additionally, if $h(\tau_1; t_1)$ is uncorrelated in the delay variable with $h(\tau_2; t_2)$, then

$$E\{h(\tau_1; t)h^*(\tau_2; t + \Delta t)\} = 0 \tag{2.4}$$

for $\tau_1 \neq \tau_2$. Consequently, the autocorrelation function assumes the form

$$R_h(\tau_1; \Delta t) = R_h(\tau_1, \tau_2; \Delta t)\delta(\tau_1 - \tau_2). \tag{2.5}$$

We drop the subscript associated with τ and simply write

$$R_h(\tau_1, \tau_2; t_1, t_2) = R_h(\tau; \Delta t)\delta(\tau). \tag{2.6}$$

Channels with autocorrelations as defined above are called wide-sense stationary uncorrelated scattering (WSSUS) channels in the open literature.

With the computed autocorrelation function, we can now find the scattering function by taking the Fourier transform of the autocorrelation function with respect to the Δt variable. The scattering function is

$$S(\tau; \lambda) = \int_{-\infty}^{\infty} R_h(\tau; \Delta t) e^{-j2\pi\lambda\Delta t} d\Delta t. \tag{2.7}$$

The scattering function estimates the average output power of the channel as a function of the time delay τ and the Doppler frequency λ. From this function, we obtain four other useful functions as illustrated in Figure 2.1:

- The Doppler power spectrum is a function obtained by integrating the scattering function with respect to τ and is given by

$$S(\lambda) = \int_{-\infty}^{\infty} S(\tau; \lambda) d\tau. \tag{2.8}$$

  The Doppler power spectrum $S(\lambda)$ quantifies the channel output power as a function of the Doppler frequency λ. The range of Doppler frequencies for which $S(\lambda)$ is nonzero is the Doppler spread B_d. A large Doppler spread results from rapid variations in the channel. Likewise, a small Doppler spread results from slow variations in the channel. Figure 2.2 is an example of a typical Doppler power spectrum plot obtained from our channel sounding experiments.

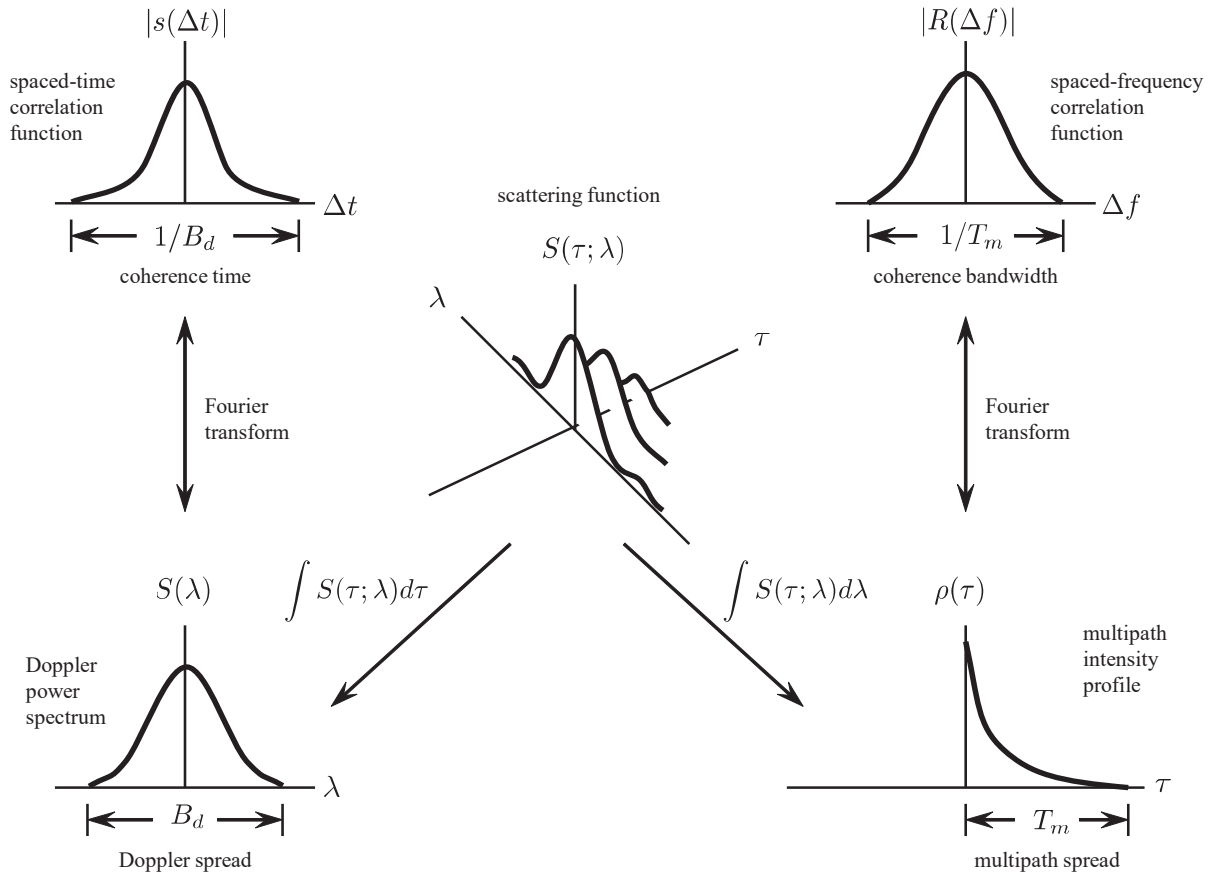

Figure 2.1: The scattering function "family tree". Adapted from [1].

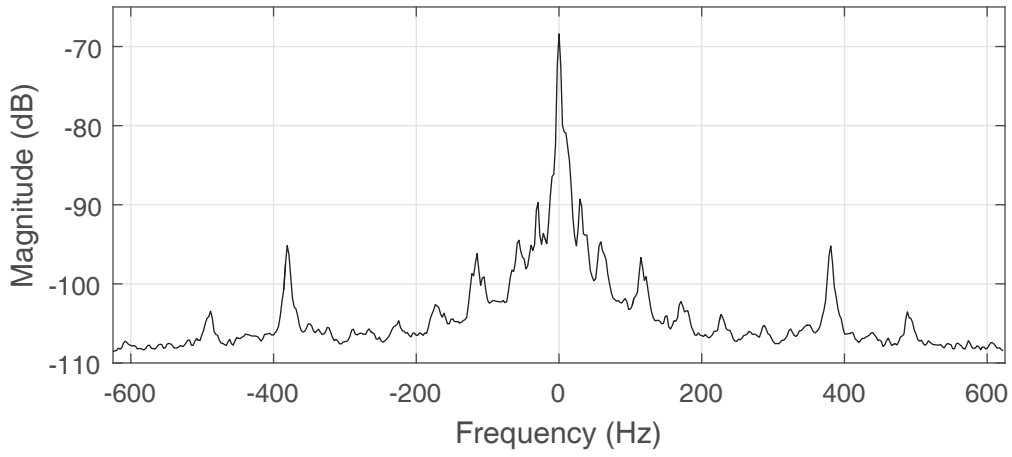

Figure 2.2: An example of the Doppler power spectrum corresponding to a multipath event on Taxiway E run at EAFB.

- The spaced-time correlation function is obtained by taking the inverse Fourier transform of the Doppler power spectrum and is expressed as

$$s(\Delta t) = \int_{-\infty}^{\infty} S(\lambda) e^{j2\pi\lambda\Delta t} d\lambda. \tag{2.9}$$

  The spaced-time correlation function quantifies how correlated the channel at time t is to the channel at $t + \Delta t$. The amount of time for which $|s(\Delta t)|$ is nonzero is called the coherence time $(\Delta t)_c$. Because $S(\lambda)$ and $s(\Delta t)$ constitute a Fourier transform pair, $(\Delta t)_c$ is approximately the reciprocal of B_d.

- The multipath intensity profile is a function obtained by integrating the scattering function with respect to the Doppler frequency λ and is given by

$$\rho(\tau) = \int_{-\infty}^{\infty} S(\tau; \lambda) d\lambda. \tag{2.10}$$

  The multipath intensity profile $\rho(\tau)$ quantifies the average power output of the channel as a function of delay τ. The maximum value of τ for which $\rho(\tau)$ is nonzero is called the multipath spread T_m. A large multipath spread means there are long powerful delays in the channel. Figure 2.3 represents a multipath intensity profile corresponding to a multipath event on Taxiway E in our channel sounding experiments.

  In analyzing the multipath intensity profile, we find it useful to look at three statistics that can readily be computed from $\rho(\tau)$ [4]: the mean excess delay, the rms delay spread and the maximum excess delay. The mean excess delay is the first moment (or mean delay) of the multipath intensity profile. i.e. the mean excess delay is given by

$$\bar{\tau} = \frac{\sum_k \rho(\tau_k)\tau_k}{\sum_k \rho(\tau_k)}, \tag{2.11}$$

  where τ_k represents the delay and $\rho(\tau_k)$ is the multipath intensity value at τ_k. The rms delay spread is the square root of the second central moment of $\rho(\tau)$, i.e.,

$$\sigma_\tau = \sqrt{\overline{\tau^2} - (\bar{\tau})^2}, \tag{2.12}$$

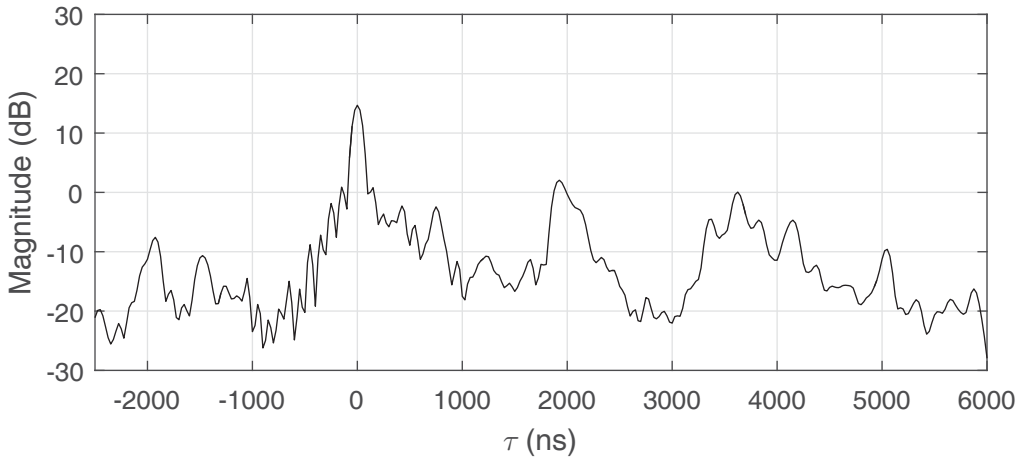

Figure 2.3: The multipath intensity profile corresponding to a multipath event on Taxiway E at EAFB.

where

$$\overline{\tau^2} = \frac{\sum_k \rho(\tau_k)\tau_k^2}{\sum_k \rho(\tau_k)}. \tag{2.13}$$

The maximum excess delay τ_{max} of $\rho(\tau)$ is defined to be the time delay at which the multipath energy falls X dB below the maximum energy. Let $\rho_{\text{max}} = \max_{\tau} \{\rho(\tau)\}$. Then

$$\tau_{\text{max}} = \underset{\tau}{\text{argmax}} \{10\log_{10}(\rho(\tau)) > 10\log_{10}(\rho_{\text{max}}) - \text{X}\}. \tag{2.14}$$

The value of X used in our computations is 20 dB.

- The spaced-frequency correlation function is a function obtained by taking the Fourier transform of the multipath intensity profile and is given by

$$R(\Delta f) = \int_{-\infty}^{\infty} \rho(\tau) e^{-j2\pi\Delta f\tau} d\tau. \tag{2.15}$$

The spaced-frequency correlation function is a measure of how correlated the channel transfer function is at two frequencies separated by Δf. This might be a useful guide in designing an orthogonal frequency division multiplexing (OFDM) system such as the OFDM mode proposed for iNET [7]. The values of Δf over which $|R(\Delta f)|$ is non-zero is the coherence bandwidth $(\Delta f)_c$ of the channel. Two OFDM subcarriers separated by more than $(\Delta f)_c$

experience uncorrelated fading. Frequency-selective fading results when $(\Delta f)_c$ is small in comparison to the signal bandwidth. Likewise, frequency-nonselective fading results when $(\Delta f)_c$ is large in comparison to the signal bandwidth. Because $\rho(\tau)$ and $R(\Delta f)$ are Fourier transform pairs, $(\Delta f)_c$ and T_m are reciprocals of each other.

2.2 Sounding Experiments at EAFB

We now present a brief description of the sounding experiments conducted at Edwards Air Force Base to which we apply the channel model described in section 2.1. A comprehensive report on this research can be found in [8].

2.2.1 The Airborne Platform

The airborne platform was a C-12 aircraft, equipped with 3 transmit antennas whose positions are illustrated in Figure 2.4. A detailed block diagram of the airborne system is illustrated in Figure 2.5. The sounding signal was switched between the three transmit antennas using the RF switch. The three switch outputs were amplified by linear RF power amplifiers and connected to the transmit antennas via hard line (heliax) cables. Antenna 2 was used to transmit both the sounding signal and the the housekeeping telemetry link as shown in Figure 2.5.

The switch controller was a custom-made FPGA based circuit that provided a 3.3 V control signal. The control signal determined which of the three output ports was connected to the input. Graphical representations of the control signals are illustrated in the next section in the context of the ground station configurations for L- and C-band. Each of the three transmit antennas was active for 50 μs in a repeating round-robin fashion. At the end of each cycle, a 50 μs blanking period was inserted by disabling all outputs. The blanking period was used for synchronizing the ground station switch. Each ground station antenna is active during a complete 200-μs-cycle.

2.2.2 Ground Station Configuration

The ground station antennas and RF hardware were located in and around Building 4795 at EAFB, California. An aerial view of Building 4795 and the antennas is shown in Figure 2.6. An alternate view of the relative positions is shown in Figure 2.7. Three physical antennas were

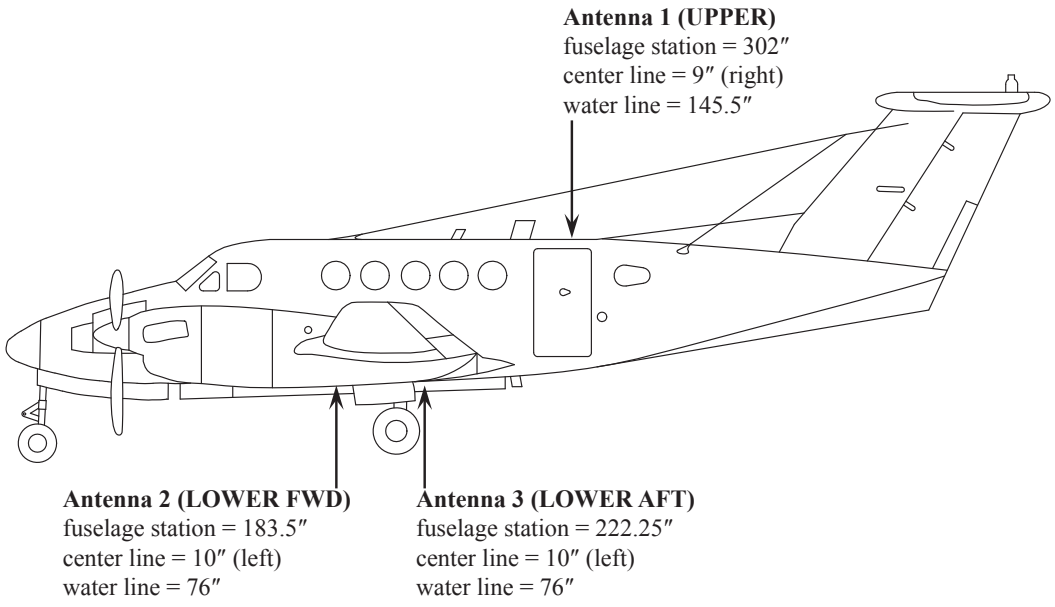

Figure 2.4: The C-12 aircraft used for the channel sounding experiments at Edwards, AFB. Also shown are the locations of the three transmit antennas used in the experiments

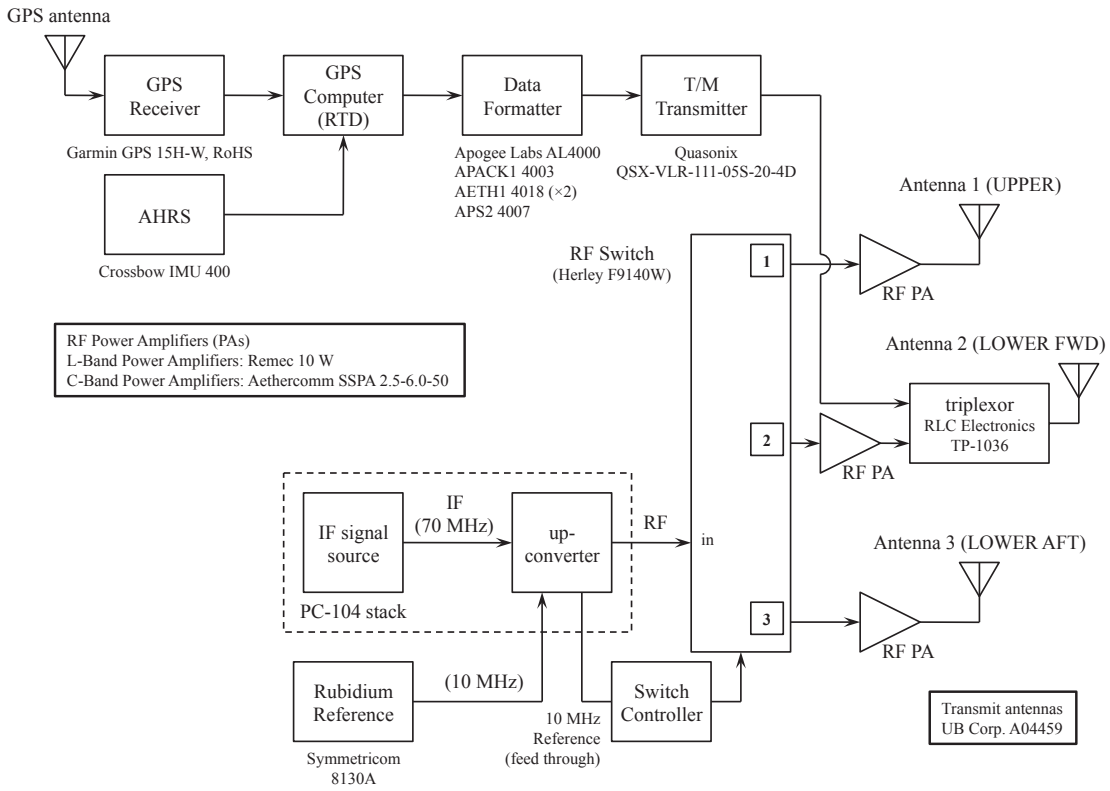

Figure 2.5: A detailed block diagram of the airborne transmitter on the C-12 aircraft.

Table 2.1: Description of the receive antennas.

Antenna	Diameter	Comments
RX1	5 m.	Building 4795 "Antenna 5" (EMT Model 150), tracking performed by conical scan, RHCP.
RX2	5 m.	Same as RX1, except LHCP is used.
RX3	8 ft.	Tracking performed by conical scan, RHCP.
RX4	4 ft.	Tracking performed by steering using GPS data downlinked from the C-12, RHCP.

involved in the channel sounding experiments. Antennas 1 and 2 were derived from the two available polarization outputs from the feed of the 5-meter parabolic reflector designated "Antenna 5" at Building 4795. Antenna 3 was an 8-foot parabolic reflector on loan from Patuxent River Naval Air Station and was situated on a trailer to the west of Antenna 5 as shown. Antenna 4 was a 4-foot parabolic reflector known as the "iNet" antenna situated on the east end of the roof of Building 4795. The properties of these antennas are summarized in Table 2.2.2.

2.2.3 System Configuration for L-Band Channel Sounding Experiments

A detailed block diagram of the ground system configuration for the L-band channel sounding experiments is shown in Figure 2.8. The outputs called Antenna 1 and Antenna 2 were derived from the right-hand-circular polarization (RHCP) and left-hand-circular polarization (LHCP) feeds, respectively, from the antenna called "Antenna 5" (at Building 4795) by the EAFB personnel. Antenna 3 and Antenna 4 were the RHCP outputs of the "Pax Antenna" and the "iNet Antenna," respectively, as shown. Gain was applied to the "Pax Antenna" and "iNet Antenna" feeds to equalize the signal levels presented to the switch input. This was done to remove the AGC effects of the M/A-Com receiver.

The RF switch applied each input to the M/A-Com 5550i receiver in a round-robin fashion and in synchronism with the transmitter switching. The relationship between the transmitter and receiver switches is illustrated in Figure 2.9. The switch output was downconverted to a 70 MHz IF by a Tyco M/A-Com 5550i receiver. The IF output was sampled at 200 Msamples/s by a

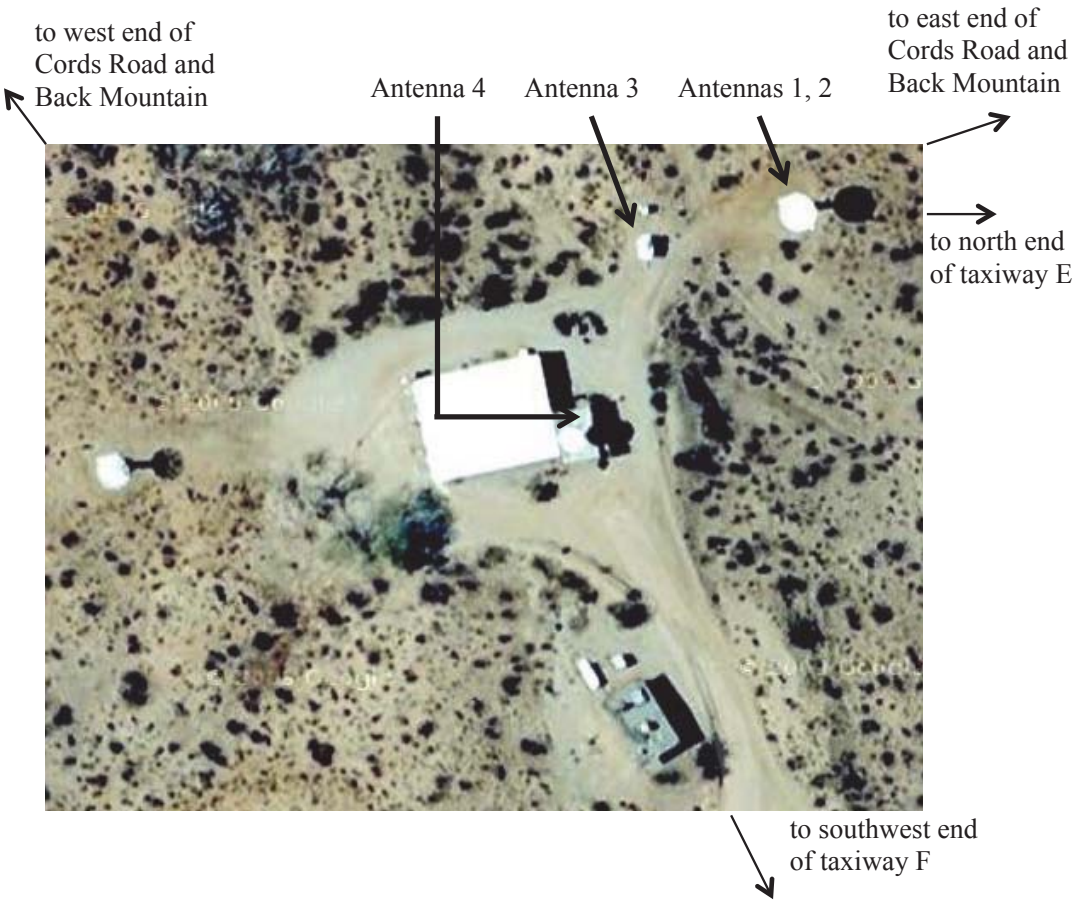

Figure 2.6: An aerial view of Building 4795 showing the positions of Antennas 1 - 4. All of the antennas were used for the L-band channel sounding experiments. Antennas 3 and 4 were used for the C-band channel sounding experiments.

Wideband Systems data acquisition system. The receiver AGC and synchronization pulse (EVT1 of Figure 2.9) were also recorded. The RHCP output of "Antenna 5" was also used to receive and demodulate the housekeeping telemetry link whose data was recorded for post-experiment analysis and for controlling the "iNet" antenna.

2.3 Scattering Functions

We now analyze impulse responses corresponding to Black Mountain East-West run, Cords Road East-West run and Taxiway North-South run at Edwards AFB, California for L-band (1824 MHz) and C-band (5124 MHz) transmissions. The Black Mountain flight path is illustrated in Figure 2.10.

Figure 2.7: The view at Building 4795 showing the relative positions of the three *physical* antennas. Antenna 4 is in the foreground on the left, Antenna 3 is on the trailer in the middle, and Antennas 1 and 2 (aka "Antenna 5") is on the right. Note that in this image, the antennas are facing north, *away* from the flight line and toward the Cords Road and Black Mountain flight paths.

For each of these 3 areas, N_t consecutive channel impulse responses were extracted. In summary, the processed data gives N_t impulse responses from which we estimate the scattering function. We use the double index notation - the n-th sample of the k-th impulse response is represented as $h(n;k)$ - in our analysis. We illustrate this in terms of the matrix $\mathbb{H}$.

$$\mathbb{H} = \begin{bmatrix} h(1;1) & h(2;1) & \cdots & h(N_t;1) \\ h(1;2) & h(2;2) & \cdots & h(N_t;2) \\ h(1;3) & h(2;3) & \cdots & h(N_t;3) \\ \vdots & \vdots & \ddots & \vdots \\ h(1;L_h) & h(2;L_h) & \cdots & h(N_t;L_h) \end{bmatrix}. \tag{2.16}$$

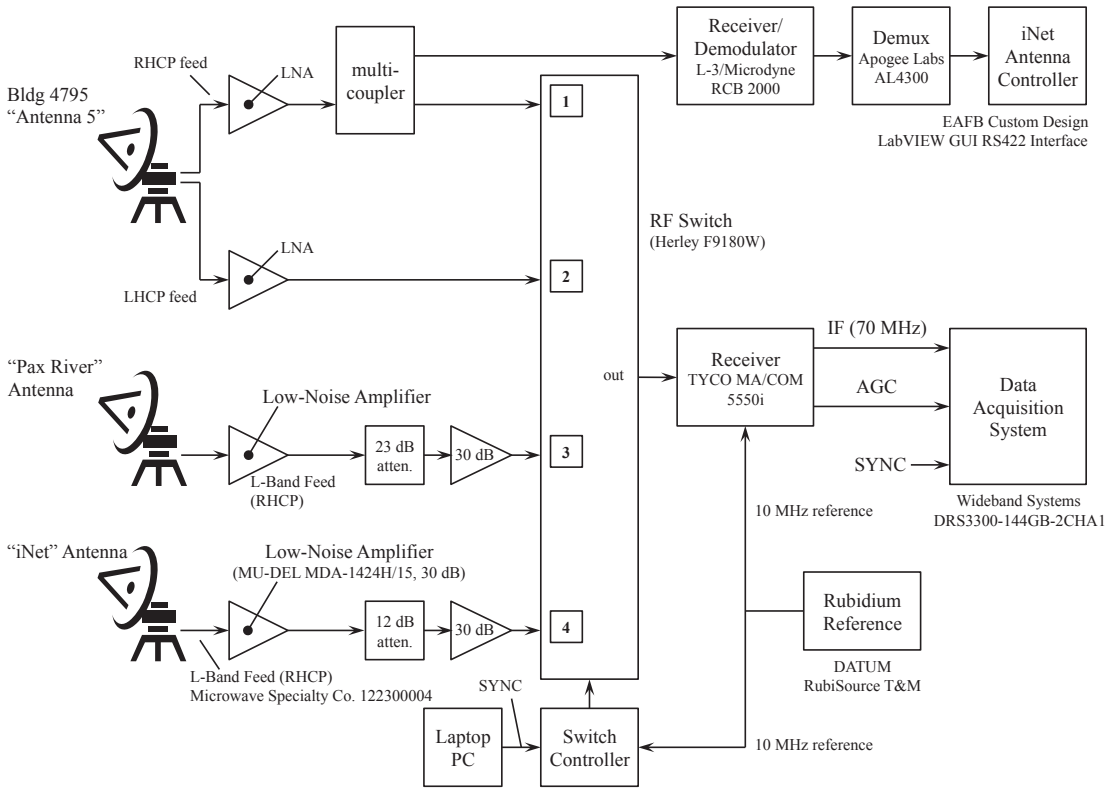

Figure 2.8: A detailed block diagram of the ground station configuration for the L-band channel sounding experiments at Edwards AFB, California.

The rows of this matrix represent the t axis. The interval between row elements is $\Delta T = 800$ μs. The columns represent the τ axis. The interval between column elements $\Delta\tau = 5$ ns.

The unbiased estimator for $R(\tau; \Delta t)$ is [3]

$$\hat{R}(n\Delta\tau; m\Delta T) = \begin{cases} \frac{1}{N_t - m} \sum_{\ell=1}^{N_t - m} h(n; \ell + m, \ell) h^*(n; \ell) & m \geq 0 \\ \frac{1}{N_t + m} \sum_{\ell=-m+1}^{N_t} h(n; \ell + m, \ell) h^*(n; \ell) & m < 0 \end{cases} \tag{2.17}$$

for $-N_t < m < N_t$. The scattering function estimate is computed using the length-N DFT of $\hat{R}(n\Delta\tau; m\Delta T)$ with respect to the second index:

$$\hat{S}(n\Delta\tau; \Delta T k/N) = \sum_{m=-N_t+1}^{N_t-1} \hat{R}(n\Delta\tau; m\Delta T) e^{-j2\pi km/N} \tag{2.18}$$

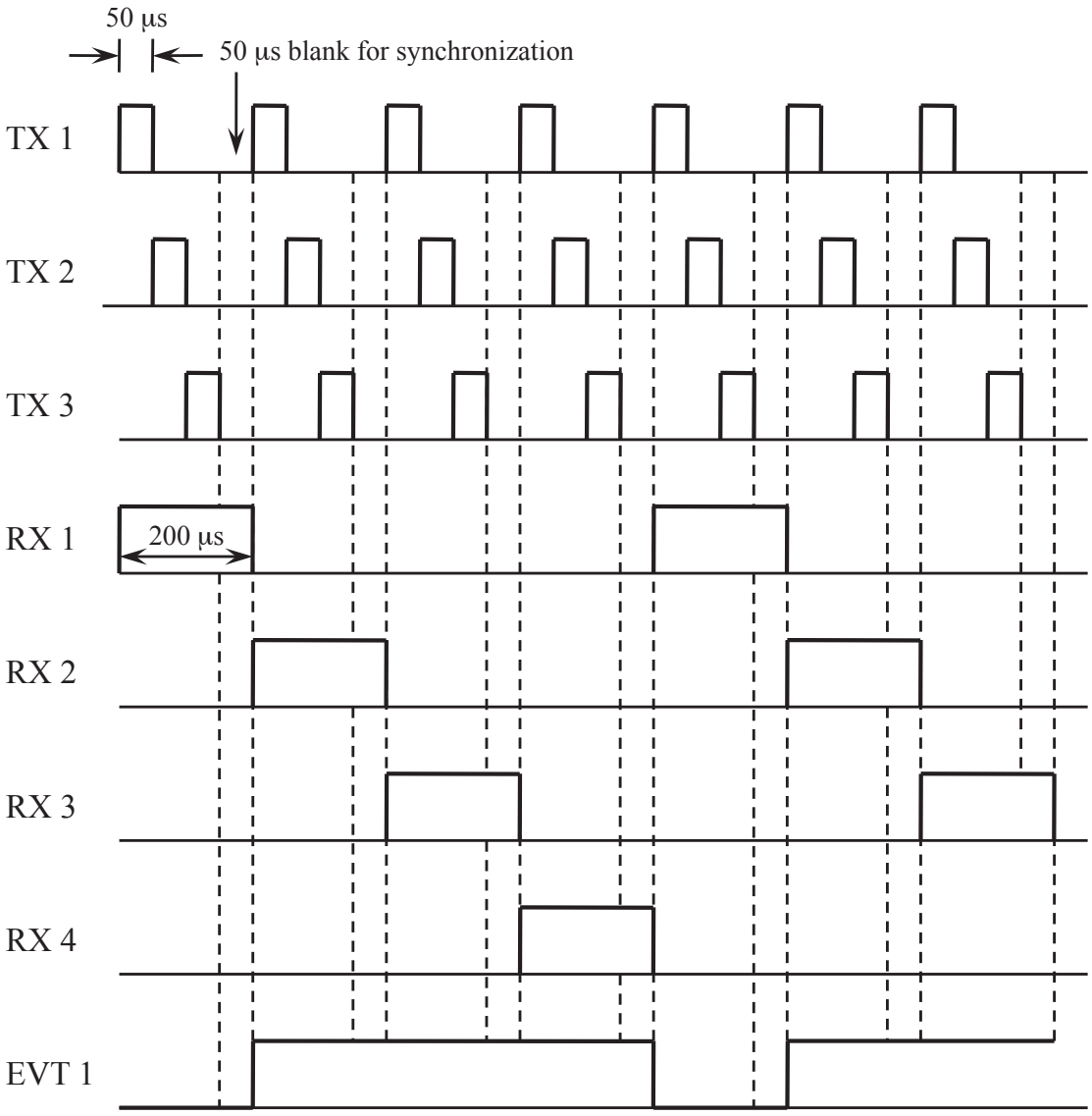

Figure 2.9: A graphical representation of the switch control used in the L-band channel sounding experiments at Edwards AFB, California.

for $0 \leq k < N$. Close examination of (2.18) shows that for a given delay (i.e. fixed n), the scattering function is an estimate of the power spectral density of the sequence

$$h(n;1), h(n;2), \ldots, h(n;N_t). \tag{2.19}$$

Consequently, well-known estimation techniques for the power spectral density, such as those described in [3,4], may be used. Nonparametric estimation techniques require the fewest assumptions

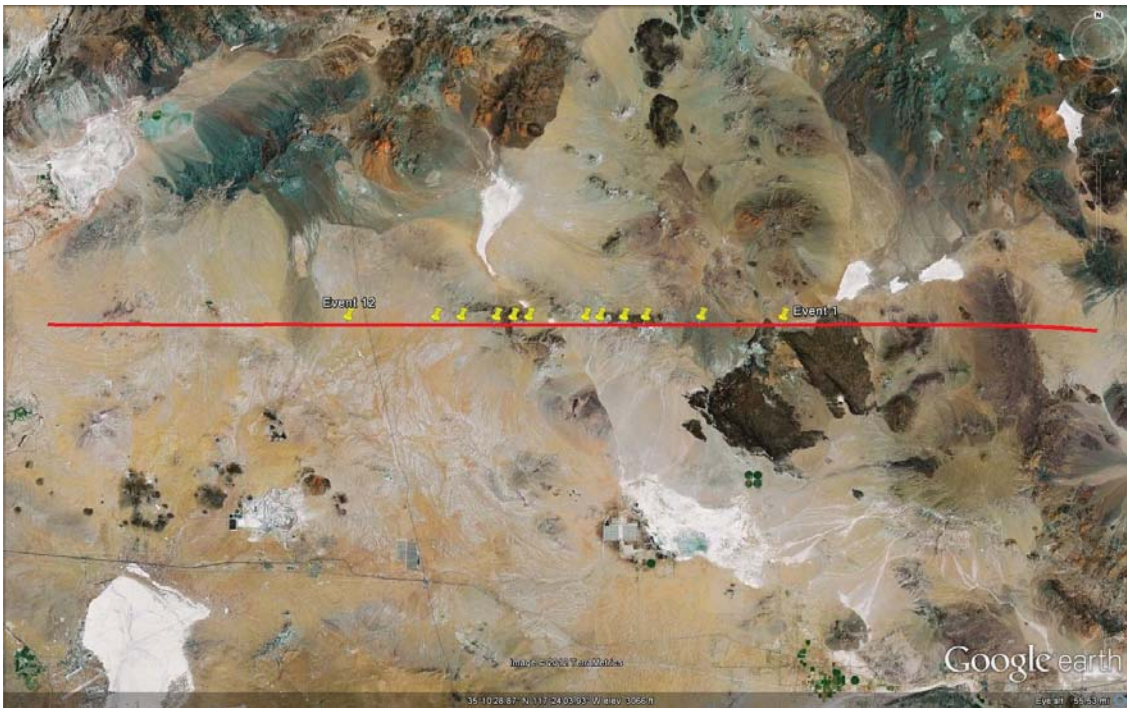

Figure 2.10: The 12 multipath events (reflection points) for the Black Mountain East-to-West run at EAFB using 1824 MHz. The yellow "thumb tack" markers indicate the multipath event locations. Event 1 is the rightmost marker and Event 12 is the left-most marker.

about the structure of the power spectral density. Welch's method for averaging modified periodograms is applied here. When Welch's method for averaging modified periodograms is applied with a 50% sequence overlap, we obtain an increase in the resolution of the power spectral density of the sequence while maintaining the same variance as Bartlett's method of spectrum estimation [3]. As a result we applied Welch's method with a Blackman window and a length $N = 512$ FFT with 50% overlap in our analysis of the captured channels.

2.4 Estimation Results

We now analyze the results connected with the areas listed above. Because of the different power levels and gains of our receivers, some engineering judgment was used in estimating the time dispersion parameters particularly for our C-Band results. We summarize our findings in Tables 2.2 - 2.7. We've used the abbreviations 'R' and 'LPD' to indicate "rapidly changing channel" and "long powerful delays", respectively.

Figure 2.11: The 3 multipath events (reflection points) for the Black Mountain East-to-West run at EAFB using 5124 MHz.

It is noted that as the plane flies alone a flight path, multipath is intermittent. Multipath occurrence is illustrated by the yellow thumb tucks depicted in Figures 2.10 and 2.11 over a short temporal window. Thus, the channel is modeled as a WSS channel because we assume the that multipath occurs over a short time span.

2.5 Summary

We have reviewed a method for generating scattering functions for the WSSUS mobile channel by first structuring our data as described in (2.16) and using Welch's periodogram to obtain the scattering function. Applying this technique to analyzing impulse response data from EAFB, we observe that because the choice of windowing function (Blackman window was used in our case) and the number of FFT points used in our modeling, we were somewhat constrained in our frequency resolution.

Figures 2.12 to 2.17 depict multipath intensity profiles and Doppler power spectra corresponding to various flight paths at EAFB using 1824 MHz and 5124 MHz transmit frequencies. We observe that the multipath intensity profiles related to significant multipath events as those shown

in Figures 2.13, 2.14 and 2.16 illustrate a strong line of sight component followed by a strong reflection with delay XX ns and power YY dB. This observation motivates a simple channel model that captures the major features of multipath propagation on test ranges:

$$h(t) = \delta(t) + a\delta(t - \tau). \tag{2.20}$$

Table 2.2: Black Mountain East-West Run using 1824 MHz transmit frequency.

Event	B_d (Hz)	$\overline{\tau}$ (ns)	σ_τ (ns)	Notes
1	4.88	1.60	99.45	
2	4.88	9.76	252.91	
3	4.88	15.35	535.29	LPD
4	4.88	35.17	900.18	
5	4.88	8.25	283.12	
6	4.88	4.02	112.65	
7	4.88	7.51	147.01	LPD
8	7.32	515.68	3645.00	R, LPD
9	4.88	12.88	156.69	
10	4.88	25.10	180.34	
11	4.88	4.24	56.39	
12	4.88	14.83	103.63	

Table 2.3: Black Mountain East-West Run using 5124 MHz transmit frequency.

Event	B_d (Hz)	$\overline{\tau}$ (ns)	σ_τ (ns)	Notes
1	4.88	1.76	82.95	
2	4.88	0.00	47.65	
3	4.88	5.144	73.24	

Table 2.4: Cords Road run using 1824 MHz transmit frequency.

Event	B_d (Hz)	$\overline{\tau}$ (ns)	σ_τ (ns)	Notes
1	4.88	29.43	812.50	
2	4.88	1.57	55.62	
3	4.88	22.06	113.25	
4	4.88	7.74	80.61	
5	4.88	13.90	80.10	

Table 2.5: Cords Road run using 5124 MHz transmit frequency.

Event	B_d (Hz)	$\overline{\tau}$ (ns)	σ_τ (ns)	Notes
1	4.88	2884.00	5514.50	LPD
2	4.88	2921.50	7404.80	LPD
3	4.88	3035.00	7331.30	LPD
4	4.88	2877.70	5439.90	LPD

Table 2.6: Taxiway run using 1824 MHz transmit frequency.

Event	B_d (Hz)	$\overline{\tau}$ (ns)	σ_τ (ns)	Notes
1	9.77	2055.40	7453.50	R,LPD
2	56.15	2601.00	3560.90	R,LPD
3	4.88	2218.50	4671.90	LPD
4	4.88	10 967.00	17 521.00	LPD
5	68.36	1682.40	5733.00	R,LPD
6	4.88	43.21	173.40	
7	4.88	2259.00	8173.80	LPD
8	4.88	318.06	1687.20	

Table 2.7: Taxiway run using 5124 MHz transmit frequency.

Event	B_d (Hz)	$\overline{\tau}$ (ns)	σ_τ (ns)	Notes
1	51.26	105.22	3752.40	R
2	4.88	7612.60	21 983.00	LPD

Analyzing the results from the tables above, we see that the Doppler spreads for the Black Mountain and Cords Road runs show little to no variability. This is largely because those flight paths do not have ample reflectors like the Taxiway path. As shown in the multipath intensity profile of Figure 2.3, the Taxiway flight path has a lot of buildings (reflectors). As such we expect to see large delays which are indicative of multipath propation. Also, because the airplane from which we are transmitting is relative to a stationary ground receiver, the propagation path constantly changes and thus we see large channel variations (i.e., large Doppler spreads) such as those shown in the Doppler power spectrum of Figure 2.17. It would be interesting to see how other frequencies other than L or S-bands behave in the flight paths used for the above modeling.

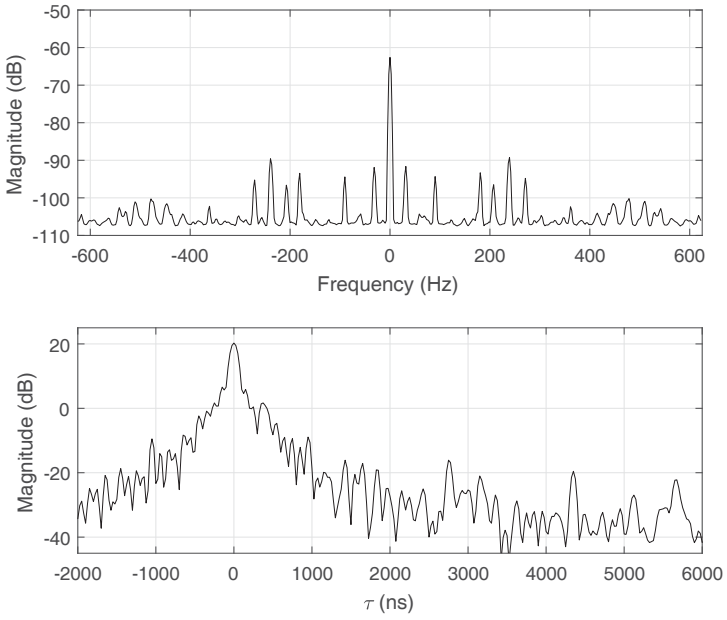

Figure 2.12: Doppler power spectrum (top) and multipath intensity profile (bottom) corresponding to a multipath event on Black Mountain at EAFB using 1824 MHz transmit frequency.

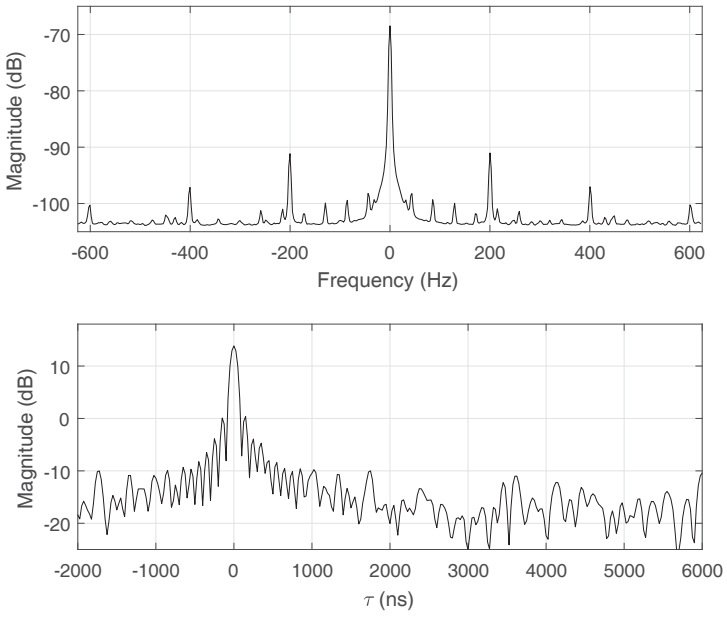

Figure 2.13: Doppler power spectrum (top) and multipath intensity profile (bottom) corresponding to a multipath event on Black Mountain at EAFB using 5124 MHz transmit frequency.

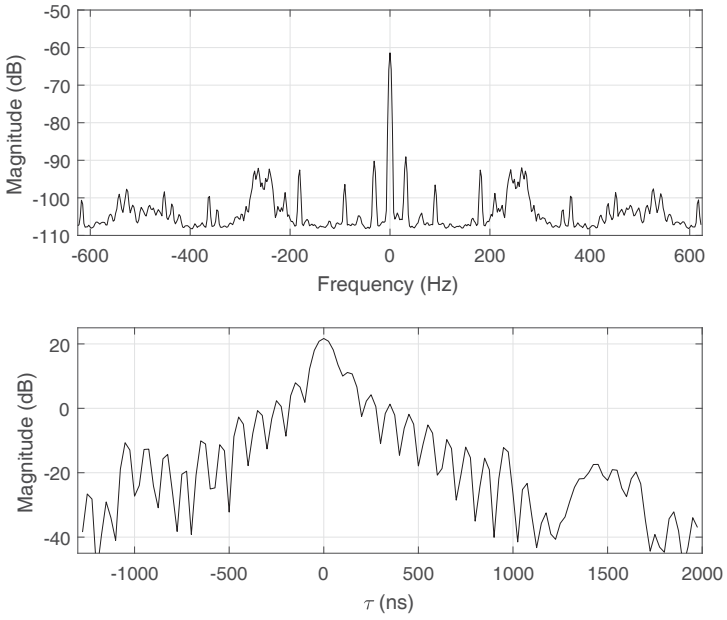

Figure 2.14: Doppler power spectrum (top) and multipath intensity profile (bottom) corresponding to a multipath event on Cords Road at EAFB using 1824 MHz transmit frequency.

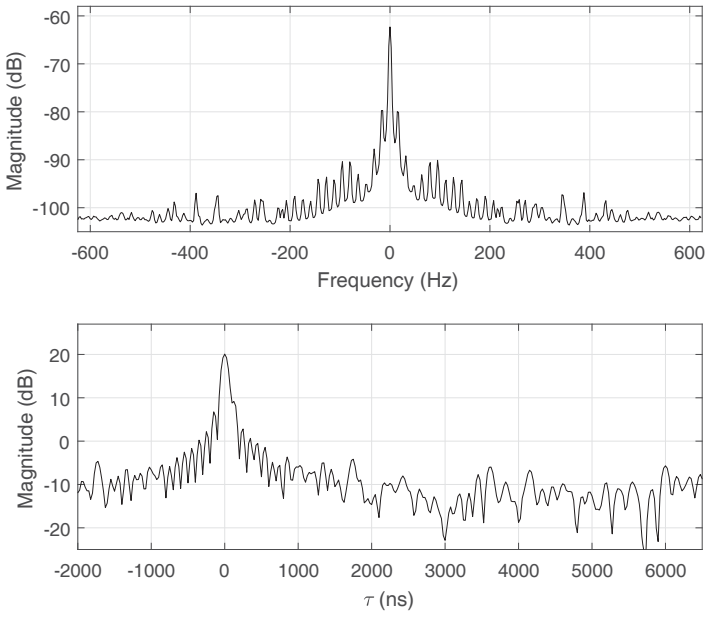

Figure 2.15: Doppler power spectrum (top) and multipath intensity profile (bottom) corresponding to a multipath event on Cords Road at EAFB using 5124 MHz transmit frequency.

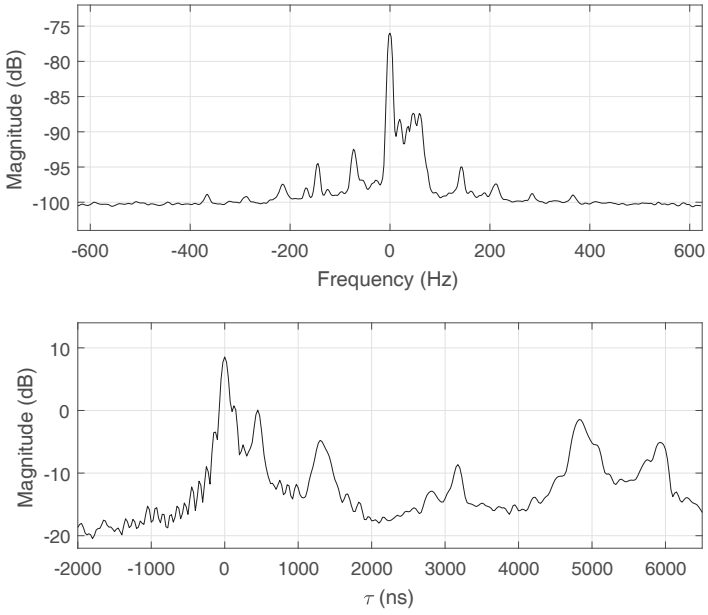

Figure 2.16: Doppler power spectrum (top) and multipath intensity profile (bottom) corresponding to a multipath event on Taxiway E at EAFB using 1824 MHz transmit frequency.

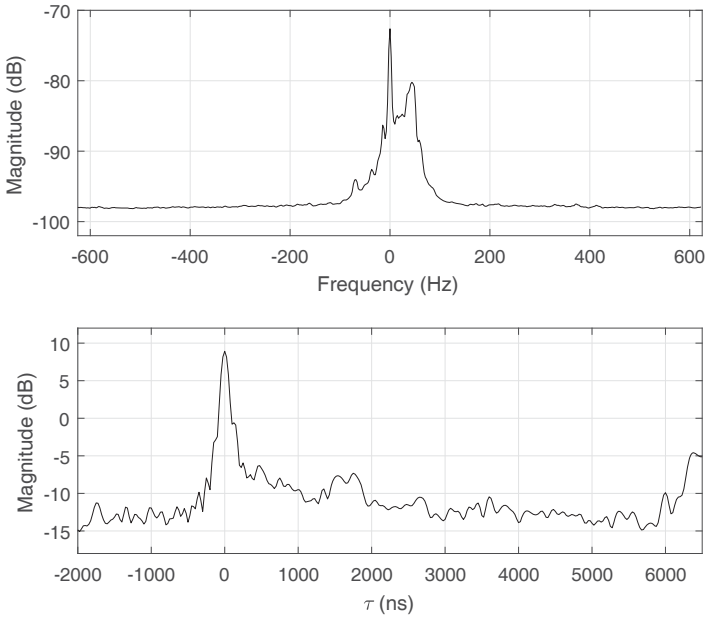

Figure 2.17: Doppler power spectrum (top) and multipath intensity profile (bottom) corresponding to a multipath event on Taxiway E at EAFB using 5124 MHz transmit frequency.

CHAPTER 3. MAXIMUM LIKELIHOOD EQUALIZATION USING SOQPSK-TG

Before proceeding, it is noteworthy to briefly discuss prior work done in this area. Perrins and Rice [9] developed a pulse amplitude modulation (PAM) representation of SOQPSK-TG over AWGN channels. Their analysis led to the design of a 4-state trellis detector which optimally detects transmitted SOQPSK-TG symbols with very minor performance losses. While their work provides invaluable insight into designing reduced complexity equalizers for partial-response ternary waveforms such as SOQPSK-TG, it necessary to explore the behavior of such approximated signal sets in multipath-induced channels.

This section examines the behavior of Perrins and Rice's PAM representation of SOQPSK-TG in a multipath channel. We first present the signal model for SOQPSK-TG and its PAM representation. We then focus on designing an optimum equalizer based on the ML principle for the approximated signal model in a multipath setting since this was not previously researched by Perrins and Rice. The resulting equations from our derivation will be used to build a trellis that operates using the Viterbi algorithm. We then test the designed ML equalizer by running simulations using Matlab to verify the validity of our analysis.

3.1 SOQPSK-TG Signal Model

SOQPSK-TG is defined as a continuous phase modulation (CPM) of the form

$$s(t, \boldsymbol{\alpha}) = Ae^{j(\phi(t,\boldsymbol{\alpha})+\phi_0)}. \tag{3.1}$$

The phase is

$$\begin{aligned}\phi(t, \boldsymbol{\alpha}) &= 2\pi h \int_{-\infty}^{t} \sum_{n=-\infty}^{k} \alpha_n g(\tau - nT_b) d\tau \\ &= 2\pi h \sum_{n=-\infty}^{k} \alpha_n q(\tau - nT_b),\end{aligned} \tag{3.2}$$

for $kT_b \leq t < (k+1)T_b$, where T_b represents the bit interval. The frequency and phase pulses are $g(t)$ and $q(t)$ respectively, with the relationship

$$q(t) = \int_{-\infty}^{t} g(\tau)d\tau. \tag{3.3}$$

The variables h and $\phi_0(t)$ are the modulation index and an arbitrary phase respectively. The modulation index h for SOQPSK-TG is equal to a $\frac{1}{2}$ and ϕ_0 can be set to 0 without any loss of generality. Additionally, $\boldsymbol{\alpha}$, associated with $\alpha_n \in \{-1, 0, 1\}$ represents ternary symbols which are related to the binary input symbols $a_n \in \{-1, 1\}$ given by

$$\alpha_n = \frac{(-1)^{n+1} a_{n-1}(a_n - a_{n-2})}{2}. \tag{3.4}$$

The binary input symbols $a_n \in \{-1, 1\}$ and the binary input bits $I_n \in \{0, 1\}$ have the relationship

$$a_n = \begin{cases} -1 & \text{for } I_n = 0 \\ +1 & \text{for } I_n = 1 \end{cases}. \tag{3.5}$$

The frequency pulse for SOQPSK-TG is a spectral raised cosine windowed by a temporal raised cosine:

$$g(t) = C \frac{\cos\left(\frac{\pi\rho Bt}{2T_b}\right)}{1 - 4\left(\frac{\rho Bt}{2T_b}\right)^2} \times \frac{\sin\left(\frac{\pi Bt}{2T_b}\right)}{\left(\frac{\pi Bt}{2T_b}\right)} \times w(t) \tag{3.6}$$

$$w(t) = \begin{cases} 1 & \text{for } 0 \leq \left|\frac{t}{2T_b}\right| < T_1 \\ \frac{1}{2}\left[1 + \cos\left(\frac{\pi}{T_2}\left(\frac{t}{2T_b} - T_1\right)\right)\right] & \text{for } T_1 \leq \left|\frac{t}{2T_b}\right| \leq T_1 + T_2 \\ 0 & \text{for } T_1 + T_2 < \left|\frac{t}{2T_b}\right| \end{cases}. \tag{3.7}$$

For SOQPSK-TG, the parameters for $g(t)$ and $w(t)$ are $\rho = 0.7$, $B = 1.25$, $T_1 = 1.5$ and $T_2 = 0.5$. The constant C is chosen to make $q(t) = \frac{1}{2}$ for $t > 2(T_1 + T_2)T_b$. The frequency and phase pulses for SOQPSK-TG are shown in Figure 3.1.

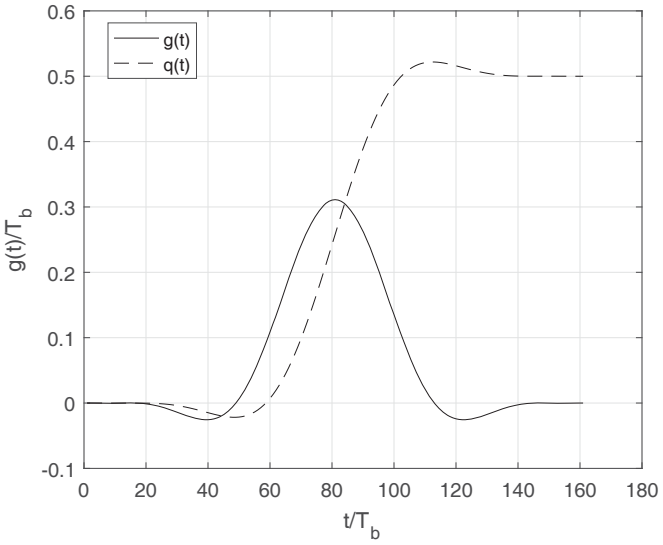

Figure 3.1: The frequency pulse $g(t)$ and the phase pulse $q(t)$ for SOQPSK-TG.

3.2 PAM Representation of SOQPSK-TG

The ML equalizer for SOQPSK-TG requires 512 states [10] in the AWGN environment. To reduce the computational complexity of the equalizer, a trellis derived from a PAM approximation of SOQPSK-TG is used. The PAM representation of SOQPSK-TG derived by Perrins and Rice [9] is

$$s(t) = \sum_{k=0}^{R-1} \sum_{i} b_{k,i} c_k(t - iT_b), \tag{3.8}$$

where $R = 2 \times 3^{L-1} = 4374$. Equation (3.8) represents SOQPSK-TG as a linear combination of 4374 pulses $c_k(t)$ whose amplitudes are modulated by pseudosymbols $b_{k,i}$. Formulae for the pulses and pseudosymbols are given in [9]. The R pseudosymbols $b_{k,i}$ are derived from the ternary SOQPSK-TG symbols α_i by a nonlinear mapping. Hence, the nonlinear nature of CPM is isolated in the pseudosymbols.

For the purposes of constructing a reduced-complexity equalizer for SOQPSK-TG, the approximation resulting from retaining the first two terms of the outer summation of (3.8) is used:

$$s(t) \approx \sum_{i} b_{0,i} c_0(t - iT_b) + \sum_{i} b_{1,i} c_1(t - iT_b), \tag{3.9}$$

where $c_0(t)$ and $c_1(t)$ are

$$c_0(t) = \left(\prod_{\ell=0}^{L-1} \psi(t + \ell T_b) \right)^2 \tag{3.10}$$

and

$$c_1(t) = 2 \left(\prod_{\ell=0}^{L-1} \psi(t + \ell T_b) \right) \left(\prod_{\ell=0}^{L-1} \psi(t + \ell T_b + Tb) \right), \tag{3.11}$$

where

$$\psi(t) = \begin{cases} \frac{\sin\left(\frac{\pi}{2} q(t)\right)}{\sin\left(\frac{\pi}{4}\right)} & 0 \le t < LT_b \\ \frac{\sin\left(\frac{\pi}{4} - \frac{\pi}{2} q(t - LT_b)\right)}{\sin\left(\frac{\pi}{4}\right)} & LT_b \le t < 2LT_b \\ 0 & \text{otherwise} \end{cases}. \tag{3.12}$$

These pulses, known as *principal pulses* [9] are plotted in Figure 3.2. Pulse $c_0(t)$ has support on $0 \le t \le 9T_b$ and pulse $c_1(t)$ has support on $0 \le t \le 8T_b$. The corresponding pseudosymbols from (3.9) are

$$b_{0,i} = \begin{cases} -je^{j\theta_{i-1}} & \alpha_i = -1 \\ e^{j\theta_{i-1}} & \alpha_i = \quad 0 \\ je^{j\theta_{i-1}} & \alpha_i = +1 \end{cases} \qquad b_{1,i} = \begin{cases} \frac{1}{\sqrt{2}}(1-j)e^{j\theta_{i-1}} & \alpha_i = -1 \\ \frac{1}{\sqrt{2}}e^{j\theta_{i-1}} & \alpha_i = \quad 0 \\ \frac{1}{\sqrt{2}}(1+j)e^{j\theta_{i-1}} & \alpha_i = +1, \end{cases} \tag{3.13}$$

where

	i even			i odd	
θ_i	I_{i-2}	I_{i-1}	θ_i	I_{i-1}	I_{i-2}
$3\pi/2$	0	0	$3\pi/2$	0	0
π	0	1	π	0	1
0	1	0	0	1	0
$\pi/2$	1	1	$\pi/2$	1	1

(3.14)

is the phase state of SOQPSK-TG at the end of bit time i. When working with the Viterbi algorithm, it is most convenient to express the pseudosymbols in the form

$$b_{0,i} = \beta_0(\alpha_i)e^{j\theta_{i-1}} \qquad b_{1,i} = \beta_1(\alpha_i)e^{j\theta_{i-1}}, \tag{3.15}$$

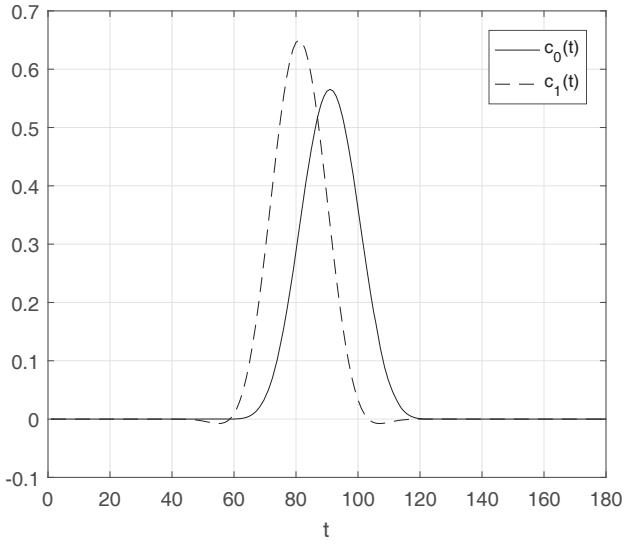

Figure 3.2: The principal pulses associated with the PAM representation of SOQPSK-TG.

where, after quick inspection of (3.13), we have

$$\beta_0(\alpha_i) = \begin{cases} -j & \alpha_i = -1 \\ 1 & \alpha_i = \quad 0 \\ j & \alpha_i = +1 \end{cases} \qquad \beta_1(\alpha_i) = \begin{cases} \frac{1}{\sqrt{2}}(1-j) & \alpha_i = -1 \\ \frac{1}{\sqrt{2}} & \alpha_i = \quad 0 \\ \frac{1}{\sqrt{2}}(1+j) & \alpha_i = +1. \end{cases} \tag{3.16}$$

We now proceed to apply the above PAM representation to develop a reduced-state trellis equalizer.

3.3 Reduced-State ML Equalizer

The reduced-state trellis equalizer follows from the ML principle. Let $\mathbf{I} = [I_0 I_1 \ldots I_{n_b-1}]$ be a sequence of n_b bits transmitted during the interval $0 \leq t \leq n_b T_b$. Using continuous-time notation for the moment, let $r(t)$ be the complex-valued baseband equivalent of the received signal at the input to the SOQPSK-TG equalizer given by

$$r(t) = s(t) * h_c(t) + n(t), \tag{3.17}$$

where $n(t)$ is a complex-valued circularly symmetric normal random process with zero mean and auto-correlation function

$$\mathbf{E}\Big\{n(t+\tau)n^*(t)\Big\} = 2N_0\delta(\tau). \tag{3.18}$$

The log-likelihood function for the symbol sequence $\mathbf{I}$ is [2]:

$$\Lambda(\mathbf{I}) = -\frac{1}{2N_0}\int_0^{n_bT_b} |r(t) - s(t) * h_c(t)|^2\, dt. \tag{3.19}$$

Using the approximation (3.9), the log-likelihood function may be expressed as

$$\begin{aligned}
\Lambda(\mathbf{I}) &\approx -\frac{1}{2N_0}\int_0^{n_bT_b}\left| r(t) - \left[\sum_{i=0}^{n_b-1} b_{0,i}c_0(t-iT_b) + \sum_{i=0}^{n_b-1} b_{1,i}c_1(t-iT_b)\right] * h_c(t)\right|^2 dt \\
&= -\frac{1}{2N_0}\int_0^{n_bT_b}\left| r(t) - \left[\sum_{i=0}^{n_b-1} b_{0,i}\underbrace{c_0(t-iT_b) * h_c(t)}_{h_0(t-iT_b)} + \sum_{i=0}^{n_b-1} b_{1,i}\underbrace{c_1(t-iT_b) * h_c(t)}_{h_1(t-iT_b)}\right]\right|^2 dt \\
&= -\frac{1}{2N_0}\int_0^{n_bT_b}\left| r(t) - \left[\sum_{i=0}^{n_b-1} b_{0,i}h_0(t-iT_b) + \sum_{i=0}^{n_b-1} b_{1,i}h_1(t-iT_b)\right]\right|^2 dt \\
&= \frac{1}{2N_0}\int_0^{n_bT_b}\Bigg(-|r(t)|^2 + 2\,\mathrm{Re}\left\{ r(t)\left[\sum_{i=0}^{n_b-1} b_{0,i}h_0(t-iT_b) + \sum_{i=0}^{n_b-1} b_{1,i}h_1(t-iT_b)\right]^*\right\} \\
&\quad - \sum_{i=0}^{n_b-1}\sum_{i'=0}^{n_b-1} b_{0,i}^*b_{0,i'}h_0^*(t-iT_b)h_0(t-i'T_b) - \sum_{i=0}^{n_b-1}\sum_{i'=0}^{n_b-1} b_{0,i}^*b_{1,i'}h_0^*(t-iT_b)h_1(t-i'T_b) \\
&\quad - \sum_{i=0}^{n_b-1}\sum_{i'=0}^{n_b-1} b_{1,i}^*b_{0,i'}h_1^*(t-iT_b)h_0(t-i'T_b) - \sum_{i=0}^{n_b-1}\sum_{i'=0}^{n_b-1} b_{1,i}^*b_{1,i'}h_1^*(t-iT_b)h_1(t-i'T_b)\Bigg) dt \\
&= 2\,\mathrm{Re}\left\{\sum_{i=0}^{n_b-1} b_{0,i}^*y_{0,i} + \sum_{i=0}^{n_b-1} b_{1,i}^*y_{1,i}\right\} - \sum_{i=0}^{n_b-1}\sum_{i'=0}^{n_b-1} b_{0,i}^*b_{0,i'}x_{00,i-i'} \\
&\quad - \sum_{i=0}^{n_b-1}\sum_{i'=0}^{n_b-1} b_{0,i}^*b_{1,i'}x_{01,i-i'} - \sum_{i=0}^{n_b-1}\sum_{i'=0}^{n_b-1} b_{1,i}^*b_{0,i'}x_{10,i-i'} - \sum_{i=0}^{n_b-1}\sum_{i'=0}^{n_b-1} b_{1,i}^*b_{1,i'}x_{11,i-i'},
\end{aligned} \tag{3.20}$$

where

$$y_{0,i} \equiv y_0(iT_b) = \int_0^{n_bT_b} r(t)h_0^*(t - iT_b)dt, \tag{3.21}$$

$$y_{1,i} \equiv y_1(iT_b) = \int_0^{n_bT_b} r(t)h_1^*(t - iT_b)dt, \tag{3.22}$$

$$x_{00,i} \equiv x_{00}(iT_b) = \int_0^{n_bT_b} h_0^*(t)h_0(t + iT_b)dt, \tag{3.23}$$

$$x_{01,i} \equiv x_{01}(iT_b) = \int_0^{n_bT_b} h_0^*(t)h_1(t + iT_b)dt, \tag{3.24}$$

$$x_{10,i} \equiv x_{10}(iT_b) = \int_0^{n_bT_b} h_1^*(t)h_0(t + iT_b)dt, \tag{3.25}$$

and

$$x_{11,i} \equiv x_{11}(iT_b) = \int_0^{n_bT_b} h_1^*(t)h_1(t + iT_b)dt, \tag{3.26}$$

with

$$\begin{aligned}\int_0^{n_bT_b} h_0^*(t - iT_b)h_0(t - i'T_b)dt &= \int_0^{n_bT_b} h_0^*(t')h_0(t' + iT_b - i'T_b)dt' \\ &= \int_0^{n_bT_b} h_0^*(t')h_0(t' + (i - i')T_b)dt'.\end{aligned} \tag{3.27}$$

Note that $|r(t)|^2$ and the constant $\frac{1}{2N_0}$ were discarded since they have no functional dependence on $\mathbf{I}$. Because (3.20) has no closed form solution for the ML bit sequence, a search must be conducted. The most efficient search algorithm for this type of structured problem is the Viterbi algorithm [2]. The Viterbi algorithm requires a recursive formulation of the log-likelihood function. This recursion lies at the heart of the Viterbi algorithm. A recursive form for the log-likelihood function is produced by examining the log-likelihood function for the sequence

$$\mathbf{I_n} = [I_0\ I_1\ \ldots\ I_n] \tag{3.28}$$

for $n \leq n_b$ given by

$$\begin{aligned}\Lambda(\mathbf{I}_n) \approx 2\,\mathrm{Re}\left\{\sum_{i=0}^{n} b_{0,i}^* y_{0,i} + \sum_{i=0}^{n} b_{1,i}^* y_{1,i}\right\} - \sum_{i=0}^{n}\sum_{i'=0}^{n} b_{0,i}^* b_{0,i'} x_{00,i-i'} \\ - \sum_{i=0}^{n}\sum_{i'=0}^{n} b_{0,i}^* b_{1,i'} x_{01,i-i'} - \sum_{i=0}^{n}\sum_{i'=0}^{n} b_{1,i}^* b_{0,i'} x_{10,i-i'} - \sum_{i=0}^{n}\sum_{i'-0}^{n} b_{1,i}^* b_{1,i'} x_{11,i-i'}.\end{aligned} \tag{3.29}$$

In the appendix, it is shown that (3.29) may be simplified to

$$\begin{aligned}\Lambda(\mathbf{I}_n) = \mathrm{Re}\left\{\sum_{i=0}^{n} b_{0,i}^* \left(2y_{0,i} - 2\sum_{m=1}^{L_x} b_{0,i-m} x_{00,m} - b_{0,i} x_{00,0} - 2\sum_{m=1}^{L_x} b_{1,i-m} x_{01,m} - b_{1,i} x_{01,0}\right)\right\} \\ + \mathrm{Re}\left\{\sum_{i=0}^{n} b_{1,i}^* \left(y_{1,i} - 2\sum_{m=1}^{L_x} b_{1,i'} x_{11,i-i'} - b_{1,i} x_{11,0} - 2\sum_{i'=1}^{L_x} b_{0,i-m} x_{10,m} - b_{0,i} x_{10,0}\right)\right\},\end{aligned} \tag{3.30}$$

where L_x is the time support for the auto- and cross-correlations. Writing (3.30) recursively gives

$$\begin{aligned}\Lambda(\mathbf{I}_n) = \Lambda(\mathbf{I}_{n-1}) \\ + \mathrm{Re}\left\{b_{0,n}^* \left(2y_{0,n} - 2\sum_{m=1}^{L_x} b_{0,n-m} x_{00,m} - b_{0,n} x_{00,0} - 2\sum_{m=1}^{L_x} b_{1,n-m} x_{01,m} - b_{1,n} x_{01,0}\right)\right\} \\ + \mathrm{Re}\left\{b_{1,n}^* \left(2y_{1,n} - 2\sum_{m=1}^{L_x} b_{1,n-m} x_{11,m} - b_{1,n} x_{11,0} - 2\sum_{m=1}^{L_x} b_{0,n-m} x_{10,m} - b_{0,n} x_{10,0}\right)\right\}.\end{aligned} \tag{3.31}$$

Equation (3.31) is called the *partial path metric* $(\mathrm{PPM})_n$ for $\mathbf{I}_n$. The *branch metric* $(\mathrm{BM})_n$ is

$$\begin{aligned}\mathrm{BM}_n = \mathrm{Re}\left\{b_{0,n}^* \left(2y_{0,n} - 2\sum_{m=1}^{L_x} b_{0,n-m} x_{00,m} - b_{0,n} x_{00,0} - 2\sum_{m=1}^{L_x} b_{1,n-m} x_{01,m} - b_{1,n} x_{01,0}\right)\right\} \\ + \mathrm{Re}\left\{b_{1,n}^* \left(2y_{1,n} - 2\sum_{m=1}^{L_x} b_{1,n-m} x_{11,m} - b_{1,n} x_{11,0} - 2\sum_{m=1}^{L_x} b_{0,n-m} x_{10,m} - b_{0,n} x_{10,0}\right)\right\}.\end{aligned} \tag{3.32}$$

Thus,

$$\mathrm{PPM}_n = \mathrm{PPM}_{n-1} + \mathrm{BM}_n. \tag{3.33}$$

Using the definitions (3.15), we have

$$\begin{aligned}\mathrm{BM}_n = \mathrm{Re}\Bigg\{ \beta_0^*(\alpha_n) e^{-j\theta_{n-1}} \Bigg(2y_{0,n} - 2\sum_{m=1}^{L_x} \beta_0(\alpha_{n-m}) e^{j\theta_{n-m-1}} x_{00,m} - \beta_0(\alpha_n) e^{j\theta_{n-1}} x_{00,0} \\ - 2\sum_{m=1}^{L_x} \beta_1(\alpha_{n-m}) e^{j\theta_{n-m-1}} x_{01,m} - \beta_1(\alpha_n) e^{j\theta_{n-1}} x_{01,0} \Bigg) \Bigg\} \\ + \mathrm{Re}\Bigg\{ \beta_1^*(\alpha_n) e^{-j\theta_{n-1}} \Bigg(2y_{1,n} - 2\sum_{m=1}^{L_x} \beta_1(\alpha_{n-m}) e^{j\theta_{n-m-1}} x_{11,m} - \beta_1(\alpha_n) e^{j\theta_{n-1}} x_{11,0} \\ - 2\sum_{m=1}^{L_x} \beta_0(\alpha_{n-m}) e^{j\theta_{n-m-1}} x_{10,m} - \beta_0(\alpha_n) e^{j\theta_{n-1}} x_{10,0} \Bigg) \Bigg\}. \end{aligned} \tag{3.34}$$

BM_n is used to construct a trellis upon which the Viterbi algorithm operates. The trellis is defined as follows:

1. The branch metric at index n is defined by the ternary symbols $\alpha_{n-L_x}, \ldots, \alpha_n$ and the phases $\theta_{n-L_x-1}, \ldots, \theta_{n-1}$.

2. Following Equations (3.4) and (3.5), $\alpha_{n-L_x}, \ldots, \alpha_n$ are defined by $I_{n-L_x-2}, \ldots, I_n$. The current bit I_n defines the state transition and the remaining bits $I_{n-L_x-2}, \ldots, I_{n-1}$ define the current state. Consequently, the trellis is defined by

$$N_s = 2^{L_x+2} \tag{3.35}$$

   states[1] each with two transitions to two possible next states.

3. The trellis is time varying [see (3.4)]. Even though the transitions associated with the even and odd states look similar diagrammatically, the phase states associated with the even and odd states are not. For even-indexed intervals ($n = 2k$) the state labels are $I_{2k-L_x-2}, \ldots, I_{2k-1}$ whereas for odd indexed intervals ($n = 2k+1$) the state labels are $I_{2k-L_x-1}, \ldots, I_{2k}$.

[1] Following (3.14), the phases $\theta_{n-L_x-1}, \ldots, \theta_{n-1}$ are defined by bits $I_{n+L_x-2}, \ldots, I_n$. But only θ_{n-1} defines the next state. The cumulative phase at the current state is embedded in the bits used as the phase state label.

4. Each transition through the state machine is represented by a *branch* in the trellis. Associated with each branch is an "input/output" pair denoted I_n/α_n. The "input" is the *n*-th bit $I_n \in \{0, 1\}$ and the "output" is the ternary symbol $\alpha_n \in \{-1, 0, +1\}$.

3.4 Illustrative Example

In light of the previous chapter's results, let us develop an ML equalizer for SOQPSK-TG in a channel with a strong multipath reflection:

$$h_c(t) = \delta(t) - 0.9\delta(t - T_b), \tag{3.36}$$

with the transfer function

$$H_c(f) = 1 - 0.9e^{-j2\pi f T_b}. \tag{3.37}$$

A plot of $H_c(f)$ and its relationship to SOQPSK-TG is given in Figure 3.3. Sampling this channel at 20 samples/bit, we compute the correlations and illustrate them in Figures 3.5 and 3.6. The composite channels $h_0(t)$ and $h_1(t)$ are depicted in Figure 3.4. A look at the downsampled cross-correlation terms $x_{01,i}$ and $x_{10,i}$ shown in Figure 3.6 reveals the need to incorporate taps from $i = -2$ to $i = 2$. This means that for this example channel, $L_x = 2$. Thus, we would need

$$N_s = 2^{L_x+2} = 2^{2+2} = 16 \text{ states} \tag{3.38}$$

to construct the trellis. This gives us 4-bits per state with the fifth bit becoming a branch label. The trellis diagram for $L_x = 2$ is shown in Figure 3.7.

3.5 Practical Considerations

While (3.32) may be algorithmically easy to implement, it is necessary to provide some contextually illuminating strategies to understanding the trellis diagram and effectively deploying it on a computational platform. In order to achieve this, we provide Figure 3.8 in conjunction with the trellis diagram to offer some helpful explanations to readers who would implement this system.

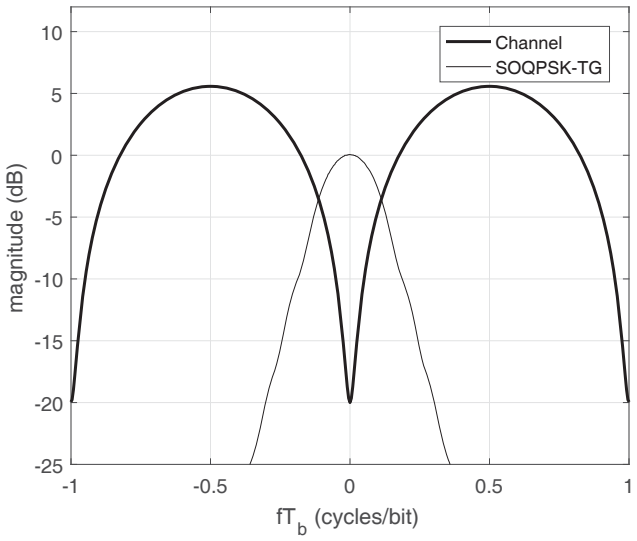

Figure 3.3: Frequency response of channel and power spectral density of SOQPSK-TG.

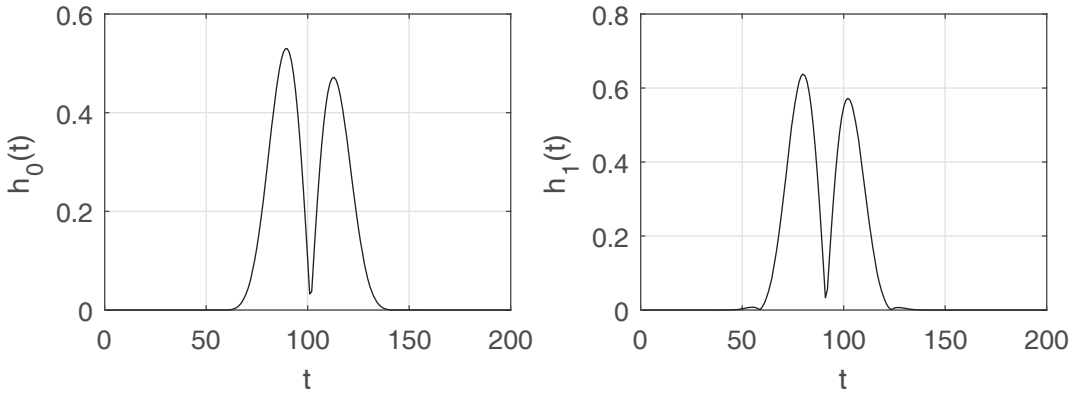

Figure 3.4: Composite channels $h_0(t)$ and $h_1(t)$.

We observe from Figure 3.8 that, for a given $x_{00,i}$, $x_{01,i}$, $x_{10,i}$, and $x_{11,i}$, the 16-state trellis operates by receiving correlation inputs $y_{0,i}$ and $y_{1,i}$ which are obtained by convolving $r(t)$ with the composite channels $h_0^*(t)$ and $h_1^*(t)$, and sampling at $t = iT_b$. All that is left is determining appropriate phase states θ_{n-3}, θ_{n-2} and θ_{n-1} (using states that precede an even-stage for example) and corresponding ternary symbols $\tilde{\alpha}_{n-2}$, $\tilde{\alpha}_{n-1}$ and $\tilde{\alpha}_n$ associated with $\beta(\tilde{\alpha}_{n-2})$, $\beta(\tilde{\alpha}_{n-1})$ and $\beta(\tilde{\alpha}_n)$ for each of the 16-states.

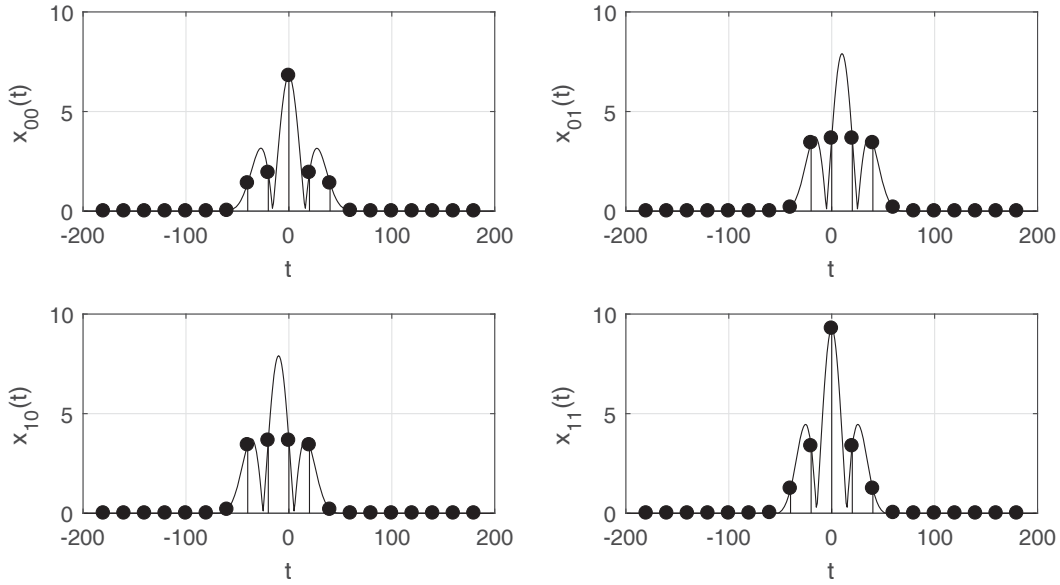

Figure 3.5: Correlations corresponding to the example channel.

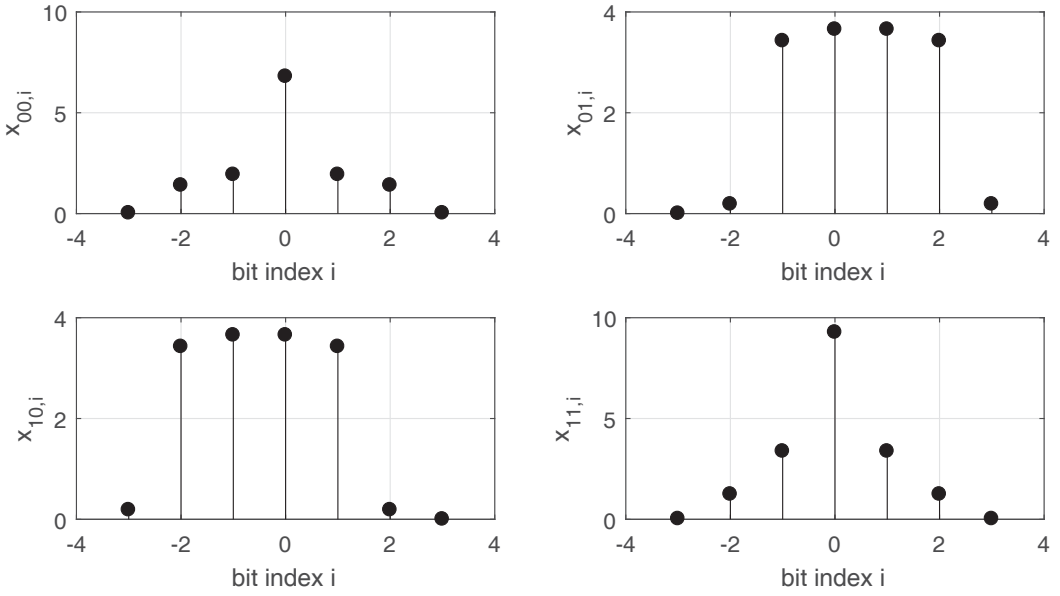

Figure 3.6: Downsampled correlations (top) x_{00} and x_{01}; (bottom) x_{10} and x_{11}.

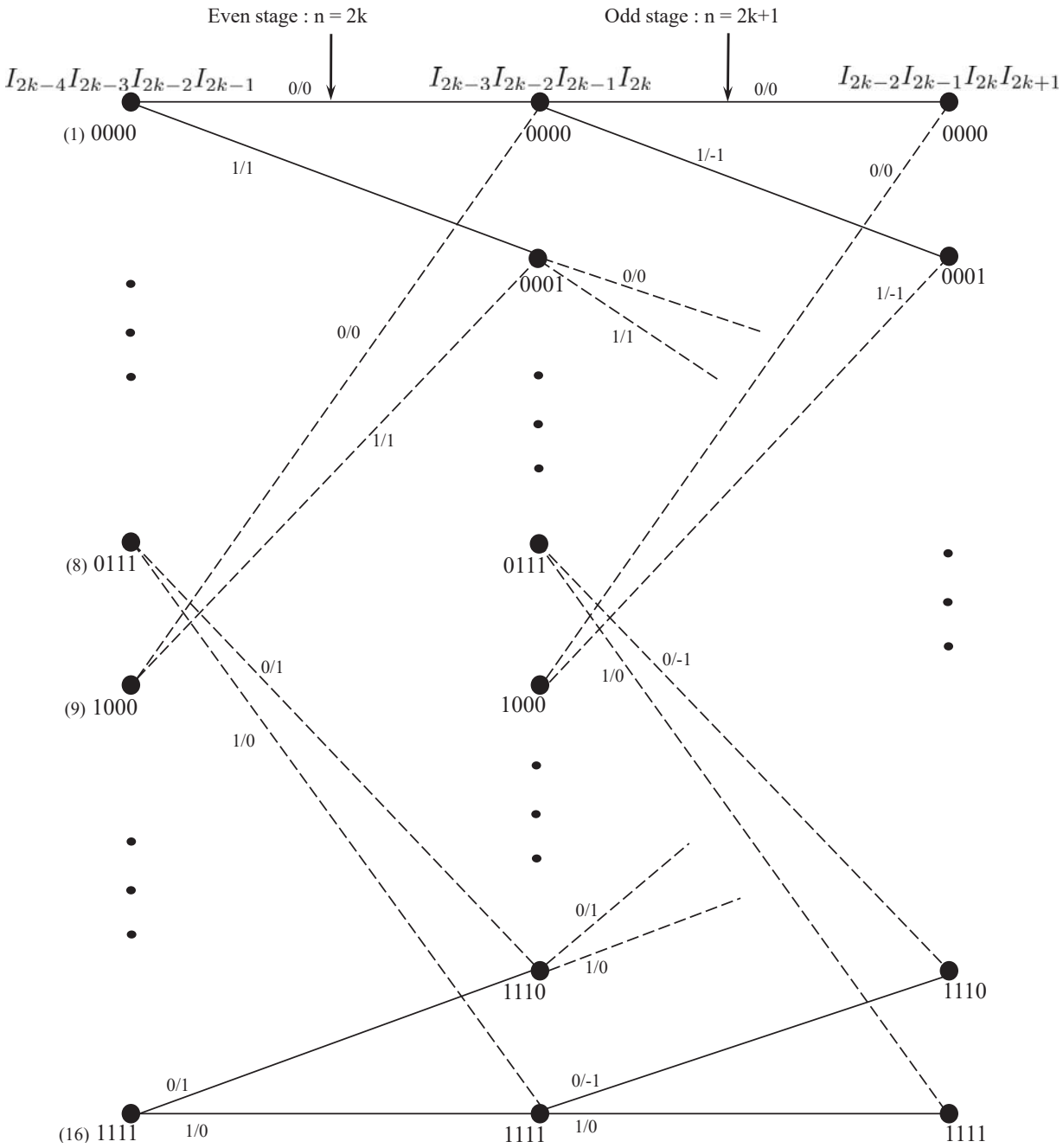

Figure 3.7: The 16-state trellis associated with the PAM representation of SOQPSK-TG transmitted through $h_c(t)$ given by (3.36).

It is critical to remember that the binary bit sequence for each state alternates between even and odd transitions. This alternation needs to be accounted for when calculating the state variables associated with each state.

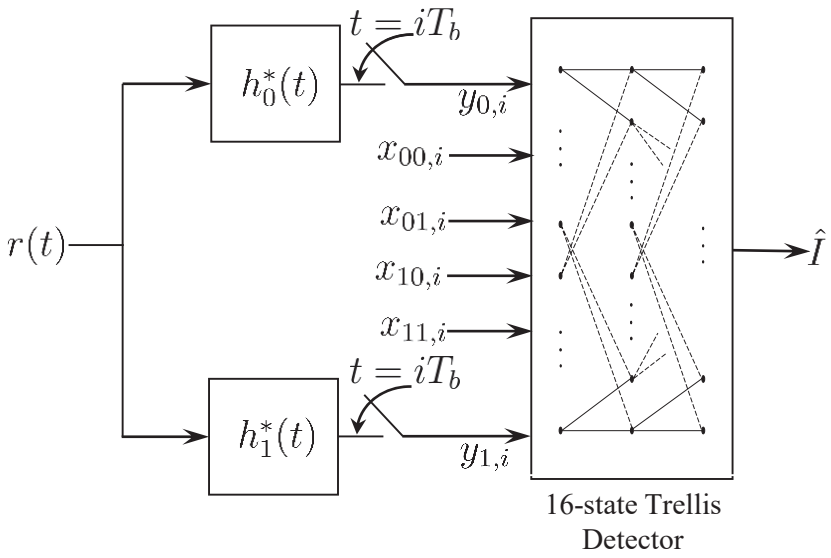

Figure 3.8: System Block Diagram.

Table 3.1: Even-indexed bit phase states

θ_{2k}	$I_{2k-2}I_{2k-1}$
$\frac{3}{2}\pi$	00
π	01
0	10
$\frac{\pi}{2}$	11

Table 3.2: Odd-indexed bit phase states

θ_{2k+1}	$I_{2k}I_{2k-1}$
$\frac{3}{2}\pi$	00
π	01
0	10
$\frac{\pi}{2}$	11

$$\alpha_{2k} = \frac{(-1)^{2k+1}a_{2k-1}(a_{2k} - a_{2k-2})}{2} = \frac{-a_{2k-1}(a_{2k} - a_{2k-2})}{2}. \tag{3.39}$$

$$\alpha_{2k+1} = \frac{(-1)^{2k+1+1}a_{2k}(a_{2k+1} - a_{2k-1})}{2} = \frac{a_{2k}(a_{2k+1} - a_{2k-1})}{2}. \tag{3.40}$$

As an illustrative example, consider state (8) with the binary bit sequence $\{0, 1, 1, 1\}$ in the trellis diagram. In order to compute the ternary symbols ($\tilde{\alpha}'s$), we first convert the binary bit sequence $\{0, 1, 1, 1\}$ into the binary input symbols $\{-1, +1, +1, +1\}$ based on (3.5). Following this, we calculate the various ternary symbols and phase states using (3.39) and (3.40), with Tables

3.1 and 3.2:

$$\tilde{\alpha}_{2k} = \frac{-(1)(-1-(1))}{2} = 1, \text{ for } I_{2k+2} = 0, \text{ even-transition;} \tag{3.41}$$

$$\tilde{\alpha}_{2k} = \frac{-(1)(1-(1))}{2} = 0, \text{ for } I_{2k+2} = 1, \text{ even-transition;} \tag{3.42}$$

$$\tilde{\alpha}_{2k-1} = \frac{(1)(1-(1))}{2} = 0, \text{ odd-transition;} \tag{3.43}$$

$$\tilde{\alpha}_{2k-2} = \frac{-(1)(1-(-1))}{2} = -1, \text{ even-transition.} \tag{3.44}$$

The phase states $\theta' s$ are given by

$$\theta_{2k-1} = \frac{\pi}{2}, \text{ since the phase state for } I_{2k}, \text{ requires } I_{2k-2}I_{2k-1}; \tag{3.45}$$

$$\theta_{2k-2} = \frac{\pi}{2}, \text{ since the phase state for } I_{2k-1}, \text{ requires } I_{2k-2}I_{2k-3}; \tag{3.46}$$

$$\theta_{2k-3} = \pi, \text{ since the phase state for } I_{2k-1}, \text{ requires } I_{2k-4}I_{2k-3}. \tag{3.47}$$

With the calculated phase states and ternary symbols and incorporating (3.15) into (3.32), recursively computing the Viterbi algorithm becomes trivial.

3.6 MMSE Equalizer

The arrangement shown in Figure 3.9 is used to represent MMSE equalization. The complex-valued baseband equivalent representation [2] is used for all signals. Starting with the block diagram of Figure 3.9 (a), the SOQPSK-TG signal $s_c(t)$ is transmitted through a channel with impulse response $h_c(t)$, the output of which, accompanied by thermal noise, forms the received signal $r(t)$. After the application of an anti-aliasing (AA) low-pass filter with impulse response $h_a(t)$, T_b-spaced samples of $r(t)$ are produced by an analog-to-digital (A/D) converter. Assuming the anti-aliasing filter does not distort the received signal, the samples of the received signal may be expressed as

$$r(n) = s(n) * h(n) + w(n) = \sum_{k=-L_1}^{L_2} h(k)s(n-k) + w(n), \tag{3.48}$$

where

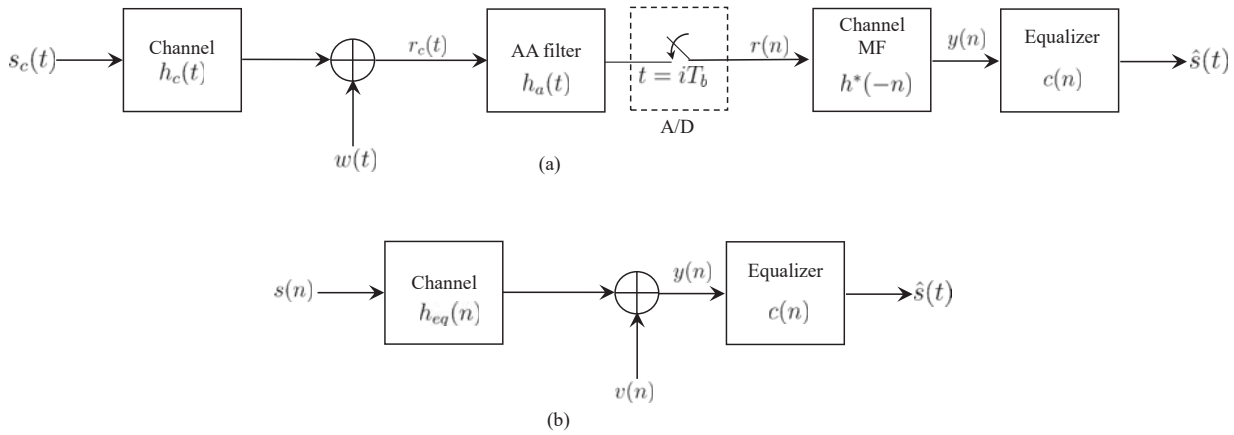

Figure 3.9: Block diagram of a system that applies MMSE equalizer to samples of received SOQPSK-TG signal: (a) system showing continuous-time signals, anti-aliasing filter, and A/D converter; (b) equivalent discrete-time system.

$$r(n) = r_c(nT_b), \qquad s(n) = s_c(nT_b), \tag{3.49}$$

$$h(n) = h_c(t) * h_a(t)\Big|_{t=nT_b}, \tag{3.50}$$

and where $w(n)$ is the nth sample in a sequence of zero-mean complex-valued Gaussian random variables with auto-correlation function

$$R_w(k) = \frac{1}{2}\mathbf{E}\Big\{w(n)w^*(n-k)\Big\} = \sigma_w^2\delta(k). \tag{3.51}$$

Note that (3.48) assumes the discrete-time channel has support on $-L_1 \le n \le L_2$. As a first step, we apply samples $r(n)$ to a filter matched to the discrete-time channel to produce $y(n)$:

$$\begin{aligned} y(n) =& r(n) * h^*(-n) \\ &= s(n) * \underbrace{h(n) * h^*(-n)}_{heq(n)} + \underbrace{w(n) * h^*(-n)}_{v(n)} \\ &= \sum_{k=-L_{eq}}^{L_{eq}} h_{eq}(k)s(n-k) + v(n), \end{aligned} \tag{3.52}$$

where $L_{eq} = L_1 + L_2$, and $v(n)$ is a complex-valued Gaussian random sequence with zero mean and auto-correlation function

$$R_v(k) = \frac{1}{2}\mathbf{E}\Big\{v(n)v^*(n-k)\Big\} = \sigma_w^2 h_{eq}(k). \tag{3.53}$$

The samples $y(n)$ form the input to an MMSE equalizer. The MMSE equalizer is a finite impulse response (FIR) filter with coefficients $c(n)$ for $-L_c \leq n \leq L_c$ designed to minimize the mean-squared error between the equalizer filter output $\hat{s}(n)$ and the sequence $s(n)$. The entire system may be represented by an equivalent discrete-time system shown in Figure 3.9 (b).

The vector of filter coefficients that minimizes the mean-squared error

$$\mathcal{E} = \mathbf{E}\Big\{ \mid s(n) - \hat{s}(n) \mid^2 \Big\} \tag{3.54}$$

is given by

$$\mathbf{c} = \left[\mathbf{G}\mathbf{R}_{s,1}\mathbf{G}^\dagger + \mathbf{R}_v\right]^{-1}\mathbf{R}_{s,2}\mathbf{g}, \tag{3.55}$$

where $\mathbf{c}$ is the $(2L_c+1)\times 1$ vector of filter coefficients. The parameters $\mathbf{G}$, $\mathbf{R}_{s,1}$, $\mathbf{R}_v$ and $\mathbf{R}_{s,2}$ are defined in [11].

3.7 Summary

Testing our analysis in Matlab, we first calculated the state variables for all even and odd transitions associated with each even and odd stage. Following this we generated the sequences $y_{0,i}$ and $y_{1,i}$ as shown in Figure 3.8. The various correlation terms were also generated and stored in appropriate vectors. A function which receives as input arguments the various state variables and correlations, including $y_{0,i}$ and $y_{1,i}$ was then used to compute the branch and partial path metrics for the derived Viterbi algorithm. We also ran simulations using an MMSE equalizer with the example channel in order to see which equalizer performs best. Figure 3.10 illustrates our findings.

As shown in Figure 3.10, the derived ML equalizer is only 1.3 dB inferior to SOQPSK-TG performance in AWGN. We also see that the ML equalizer clearly outperforms the MMSE equalizer. It is critical to recognize from Figure 3.10 that as the length of the MMSE equalizer increases beyond spanning 15 bit intervals, one observes "diminishing returns". Consequently, it

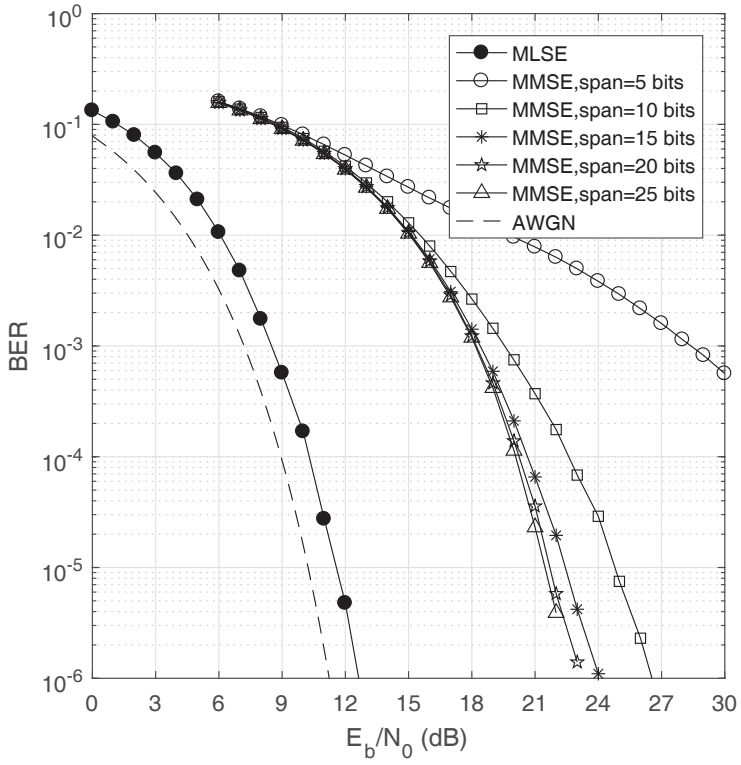

Figure 3.10: Bit error rate performance from simulations.

is almost certain that the MMSE equalizer is not capable of matching the performance of the ML equalizer. This finding is very significant since engineers and other scientists in the telemetry space can readily apply this ML equalizer to their designs. The benefits of accurate SOQPSK-TG signal detection using this ML equalizer comes at a cost of intense and expensive computation which might be regarded by some as disadvantageous. However, in light of computer processor power rapidly increasing yearly, the 16-state ML equalizer presented in this thesis could potentially be ubiquitous in the telemetry community in the foreseeable future.

CHAPTER 4. CONCLUSIONS

Based on the statistical assumptions made for WSSUS channels, multiple impulse response data was captured using 1824 MHz and 5124 MHz transmit frequencies for various locations at EAFB. Generating scattering functions for the impulse response data and obtaining the corresponding Doppler power spectrum and multipath intensity profile, we were able to characterize the mobile radio channel at EAFB and obtained some insight into the propagation of signal delay and other variations in the channels considered. Simulation results showed that test range channels usually exhibit a strong line-of-sight signal component and a strong multipath component. With this understanding, a simple channel was created to test a reduced-state ML equalizer for a PAM approximation of SOQPSK-TG. Our results show that this ML equalizer's performance is superior to filter-based equalizers for SOQPSK-TG such as MMSE equalizers.

4.1 Contributions

The formulation used in the channel characterizations depends heavily on prior work done by [6] and from chapters from [2] and [4]. Concepts from [6] focused on scattering functions for a suburban radio environment. It was thus helpful to characterize channels at other locations such as test ranges in order to obtain models that are well-suited for such areas. Additionally, drawing heavily from concepts described in [2] and [4], we see that we can obtain some insight into signal delay propagation for a given channel and also, to a reasonable degree, understand how the radio channel changes overtime.

Further, the work done by [9] was very instrumental in designing an ML detector for SOQPSK-TG using a simple channel motivated by the statistical characterization described. The utility found in [9] lies in designing a reduced state trellis detector using an approximation of a spectrally efficient waveform such as SOQPSK-TG. The implications from the analysis derived

from this research ensures the design of detectors that are relatively simple and computationally less intensive.

4.2 Further Work

Additional work is possible for characterizing multipath propagation using frequencies other than L and S-bands. Regarding the design of the ML equalizer for the PAM approximation, it would be helpful to examine and test more channel models other than the simple case looked at in this thesis. It would be interesting to assess the performance degradation for longer channels where the correlations are truncated to $L_x = 2$.

REFERENCES

[1] B. Sklar, "Rayleigh fading channels in mobile digital communication systems part I: Characterization," *IEEE Communications Magazine*, vol. 35, pp. 90 – 100, July 1997. vii, 6

[2] J. Proakis and M. Salehi, *Digital Communications*. New York: McGraw-Hill, fifth ed., 2008. 1, 4, 28, 29, 37, 41

[3] M. Hayes, *Statistical Digital Signal Processing and Modeling*. New York: John Wiley & Sons, 1996. 1, 14, 16

[4] T. Rappaport, *Wireless Communications, Principles and Practice*. Upper Saddle River, NJ: Prentice-Hall, second ed., 2002. 1, 7, 41

[5] Secretariat, Range Commanders Council, White Sands Missile Range, New Mexico, *IRIG Standard 106-09: Telemetry Standards*, 2009. (Available on-line at http://www.irig106.org/docs/106-09). 2

[6] H. Hashemi, *Simulation of the Urban Radio Propagation Channel*. PhD thesis, University of California, Berkeley, Berkeley, CA, 1977. 4, 41

[7] integrated Network Enhanced Telemetry (iNET) Radio Access Network Standards Working Group, "Radio access network (RAN) standard, version 0.7.9," tech. rep. Available at `https://www.tena-sda.org/display/INET/iNET+Platform+Interface+Standards`. 8

[8] M. Rice, "Final report: Multipath modeling and mitigation using multiple antennas (m4a)," tech. rep., Brigham Young University, 2012. 9

[9] E. Perrins and M. Rice, "PAM representation of ternary CPM," *IEEE Transactions on Communications*, vol. 56, pp. 2020–2024, December 2008. 23, 25, 26, 41

[10] M. Geoghegan, "Implementation and performance results for trellis detection of SOQPSK," in *Proceedings of the International Telemetering Conference*, (Las Vegas, NV), October 2001. 25

[11] M. Rice, M. Afran, and M. Saquib, "Equalization in aeronautical telemetry using multiple transmit antennas," *IEEE Transactions on Aerospace and Electronic Systems*, vol. 51, pp. 2148–2165, 7 2015. 39

APPENDIX A. BRANCH METRIC DERIVATION

As was discussed in Chapter 3, we present a rigorous development of the mathematical framework upon which the ML equalizer depends. We first look at an in-depth derivation of the branch metric following which the equivalent discrete-time model for the PAM approximation of SOPSK-TG is analyzed. Lastly, we probe into the operational structure of the ML equalizer to gain a better understanding of its functionality.

A.1 Derivation

The starting point is Equation (3.20), repeated here as Equation (A.1) for convenience:

$$\Lambda(\mathbf{I}) = 2\,\mathrm{Re}\left\{\sum_{i=0}^{n_b-1} b_{0,i}^* y_{0,i} + \sum_{i=0}^{n_b-1} b_{1,i}^* y_{1,i}\right\} - \sum_{i=0}^{n_b-1}\sum_{i'=0}^{n_b-1} b_{0,i}^* b_{0,i'} x_{00,i-i'} - \sum_{i=0}^{n_b-1}\sum_{i'=0}^{n_b-1} b_{0,i}^* b_{1,i'} x_{01,i-i'} - \sum_{i=0}^{n_b-1}\sum_{i'=0}^{n_b-1} b_{1,i}^* b_{0,i'} x_{10,i-i'} - \sum_{i=0}^{n_b-1}\sum_{i'=0}^{n_b-1} b_{1,i}^* b_{1,i'} x_{11,i-i'}, \quad \text{(A.1)}$$

where

$$x_{00,i} = x_{00}(iT_b) = \int_{-\infty}^{\infty} h_0(t+iT_b)h_0^*(t)dt \quad \text{(A.2)}$$

$$x_{01,i} = x_{01}(iT_b) = \int_{-\infty}^{\infty} h_0(t+iT_b)h_1^*(t)dt \quad \text{(A.3)}$$

$$x_{10,i} = x_{10}(iT_b) = \int_{-\infty}^{\infty} h_1(t+iT_b)h_0^*(t)dt \quad \text{(A.4)}$$

$$x_{11,i} = x_{11}(iT_b) = \int_{-\infty}^{\infty} h_1(t+iT_b)h_1^*(t)dt. \quad \text{(A.5)}$$

Note that $x_{00}(\tau) = x_{00}^*(-\tau)$, $x_{11}(\tau) = x_{11}^*(-\tau)$, and

$$x_{10}(\tau) = \int_{-\infty}^{\infty} h_1(t+\tau)h_0^*(t)dt \quad \text{(A.6)}$$

$$= \left[\int_{-\infty}^{\infty} h_1^*(t+\tau) h_0(t) dt \right]^*$$
$$= \left[\int_{-\infty}^{\infty} h_0(u-\tau) h_1^*(u) du \right]^*$$
$$= x_{01}^*(-\tau). \tag{A.7}$$

We now simplify (A.1). Starting with the second term on the right-hand side of (A.1), we partition the inner sum into the values i' for which the subscript on x_{00} is positive, zero, and negative:

$$\sum_{i=0}^{n_b-1} \sum_{i'=0}^{n_b-1} b_{0,i}^* b_{0,i'} x_{00,i-i'} = \sum_{i=0}^{n_b-1} \left[\sum_{i'=0}^{i-1} b_{0,i}^* b_{0,i'} x_{00,i-i'} + b_{0,i}^* b_{0,i} x_{00,0} + \sum_{i'=i+1}^{n_b-1} b_{0,i}^* b_{0,i'} x_{00,i-i'} \right] \tag{A.8}$$
$$= \sum_{i=1}^{n_b-1} \sum_{i'=0}^{i-1} b_{0,i}^* b_{0,i'} x_{00,i-i'} + \sum_{i=0}^{n_b-1} b_{0,i}^* b_{0,i} x_{00,0} + \sum_{i=0}^{n_b-2} \sum_{i'=i+1}^{n_b-1} b_{0,i}^* b_{0,i'} x_{00,i-i'}. \tag{A.9}$$

Note that the lower limit of the outer sum of the first term in (A.9) has been changed to 1 and the upper limit of the outer sum of the third term in (A.9) has been changed to $n_b - 2$ so as not to double-count the $i = i'$ terms. The third term in (A.9) is of the form

$$\sum_{i=0}^{n_b-2} \sum_{i'=i+1}^{n_b-1} F(i, i'). \tag{A.10}$$

The order of summation is exchanged with the aid of Figure A.1. Switching the order of summation on the the third term of (A.9) produces

$$\sum_{i=0}^{n_b-2} \sum_{i'=i+1}^{n_b-1} b_{0,i}^* b_{0,i'} x_{00,i-i'} = \sum_{i'=1}^{n_b-1} \sum_{i=0}^{i'-1} b_{0,i}^* b_{0,i'} x_{00,i-i'} \tag{A.11}$$
$$= \sum_{i'=1}^{n_b-1} \sum_{i=0}^{i'-1} b_{0,i}^* b_{0,i'} x_{00,i'-i}^* \tag{A.12}$$
$$= \left[\sum_{i'=1}^{n_b-1} \sum_{i=0}^{i'-1} b_{0,i} b_{0,i'}^* x_{00,i'-i} \right]^*, \tag{A.13}$$

which is the complex-conjugate of the first term in (A.9). Consequently, the second term on the right-hand side of (A.1) may be expressed as

$$\sum_{i=0}^{n_b-1}\sum_{i'=0}^{n_b-1} b_{0,i}^* b_{0,i'} x_{00,i-i'} = 2\,\mathrm{Re}\left\{\sum_{i=1}^{n_b-1}\sum_{i'=0}^{i-1} b_{0,i}^* b_{0,i'} x_{00,i-i'}\right\} + \sum_{i=0}^{n_b-1} b_{0,i}^* b_{0,i} x_{00,0}. \tag{A.14}$$

The final step to produce the most useful form is to use the substitution $m = i - i'$ in the first term on the right-hand side of (A.14) The substitution produces

$$\sum_{i=0}^{n_b-1}\sum_{i'=0}^{n_b-1} b_{0,i}^* b_{0,i'} x_{00,i-i'} = 2\,\mathrm{Re}\left\{\sum_{i=1}^{n_b-1}\sum_{m=1}^{i} b_{0,i}^* b_{0,i-m} x_{00,m}\right\} + \sum_{i=0}^{n_b-1} b_{0,i}^* b_{0,i} x_{00,0}. \tag{A.15}$$

The usual case is for $x_{00,m} = 0$ for $m > L_{00}$ for some integer $L_{00} \ll n_b$. In this case, the upper limit on inner summation of the first term on the right-hand side of (A.15) is $\min\{i, L_{00}\}$. If $b_{0,k} = 0$ for $k < 0$, then the more notationally simple

$$\sum_{i=0}^{n_b-1}\sum_{i'=0}^{n_b-1} b_{0,i}^* b_{0,i'} x_{00,i-i'} = 2\,\mathrm{Re}\left\{\sum_{i=1}^{n_b-1}\sum_{m=1}^{L_{00}} b_{0,i}^* b_{0,i-m} x_{00,m}\right\} + \sum_{i=0}^{n_b-1} b_{0,i}^* b_{0,i} x_{00,0} \tag{A.16}$$

may be used.

The fifth term on the right-hand side of (A.1) is simplified in the identical manner: the inner summation is partitioned as before, the order of summation is exchanged on the term corresponding to negative subscripts of x_{11} (cf. Figure A.1), and the conjugate symmetry of x_{11} is applied to produce

$$\sum_{i=0}^{n_b-1}\sum_{i'=0}^{n_b-1} b_{1,i}^* b_{1,i'} x_{11,i-i'} = 2\,\mathrm{Re}\left\{\sum_{i=1}^{n_b-1}\sum_{i'=0}^{i-1} b_{1,i}^* b_{1,i'} x_{11,i-i'}\right\} + \sum_{i=0}^{n_b-1} b_{1,i}^* b_{1,i} x_{11,0}. \tag{A.17}$$

Using the substitution $m = i - i'$ in the first term on the right-hand side of (A.17) produces

$$\sum_{i=0}^{n_b-1}\sum_{i'=0}^{n_b-1} b_{1,i}^* b_{1,i'} x_{11,i-i'} = 2\,\mathrm{Re}\left\{\sum_{i=1}^{n_b-1}\sum_{m=1}^{i} b_{1,i}^* b_{1,i-m} x_{11,m}\right\} + \sum_{i=0}^{n_b-1} b_{1,i}^* b_{1,i} x_{11,0}. \tag{A.18}$$

As before, it is usually the case that $x_{11,m} = 0$ for $m > L_{11}$ for some integer $L_{11} \ll n_b$. Consequently, the upper limit on the inner summation on the first term on the right-hand side of (A.18)

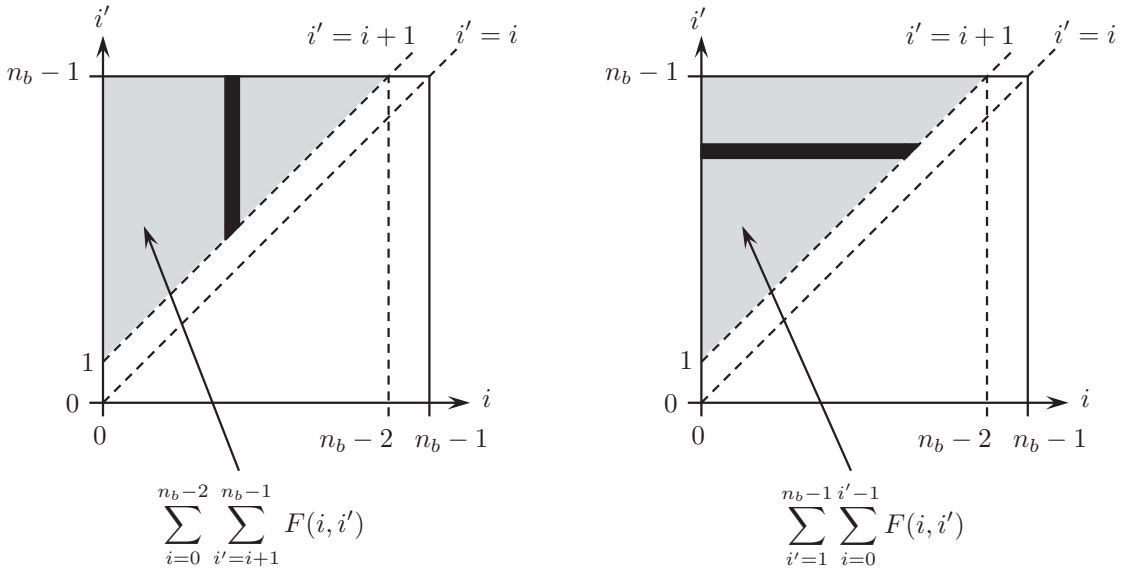

Figure A.1: A graphical representation of double summation (A.10): (left) the inner summation is with respect to i' and the outer summation is with respect to i to sum along columns of the shaded region; (right) the inner summation is with respect to i and the outer summation is with respect to i' to sum along the rows of the shaded region.

is $\min\{i, L_{11}\}$. If $b_{1,k} = 0$ for $k < 0$, then the more notationally simple

$$\sum_{i=0}^{n_b-1} \sum_{i'=0}^{n_b-1} b_{1,i}^* b_{1,i'} x_{11,i-i'} = 2\,\mathrm{Re}\left\{ \sum_{i=1}^{n_b-1} \sum_{m=-1}^{L_{11}} b_{1,i}^* b_{1,i-m} x_{11,m} \right\} + \sum_{i=0}^{n_b-1} b_{1,i}^* b_{1,i} x_{11,0} \tag{A.19}$$

may be used.

The third and fourth terms on the right-hand side of (A.1) simplify in combination. Starting with the third term on the right-hand side of (A.1), we follow the same steps as before. Partitioning the inner summation for values of i' that produce positive, zero, and negative subcripts on x_{01} gives

$$\sum_{i=0}^{n_b-1} \sum_{i'=0}^{n_b-1} b_{0,i}^* b_{1,i'} x_{01,i-i'} = \sum_{i=0}^{n_b-1} \left[\sum_{i'=0}^{i-1} b_{0,i}^* b_{1,i'} x_{01,i-i'} + b_{0,i}^* b_{1,i} x_{01,0} + \sum_{i'=i+1}^{n_b-1} b_{0,i}^* b_{1,i'} x_{01,i-i'} \right] \tag{A.20}$$

$$= \sum_{i=1}^{n_b-1} \sum_{i'=0}^{i-1} b_{0,i}^* b_{1,i'} x_{01,i-i'} + \sum_{i=0}^{n_b-1} b_{0,i}^* b_{1,i} x_{01,0} + \sum_{i=0}^{n_b-2} \sum_{i'=0}^{i-1} b_{0,i}^* b_{1,i'} x_{01,i-i'}. \tag{A.21}$$

The third term of (A.21) is of the form (A.10). Exchanging the order of summation produces (cf. Figure A.1)

$$\sum_{i=0}^{n_b-2}\sum_{i'=0}^{i-1} b_{0,i}^* b_{1,i'} x_{01,i-i'} = \sum_{i'=1}^{n_b-1}\sum_{i=0}^{i'-1} b_{0,i}^* b_{1,i'} x_{01,i-i'} \tag{A.22}$$

$$= \sum_{i'=1}^{n_b-1}\sum_{i=0}^{i'-1} b_{0,i}^* b_{1,i'} x_{10,i'-i}^* \tag{A.23}$$

$$= \left[\sum_{i'=1}^{n_b-1}\sum_{i=0}^{i'-1} b_{0,i} b_{1,i'}^* x_{10,i'-i}\right]^*, \tag{A.24}$$

where the second step used the relationship (A.7). Substituting (A.24) into (A.21) produces

$$\sum_{i=0}^{n_b-1}\sum_{i'=0}^{n_b-1} b_{0,i}^* b_{1,i'} x_{01,i-i'}$$

$$= \sum_{i=1}^{n_b-1}\sum_{i'=0}^{i-1} b_{0,i}^* b_{1,i'} x_{01,i-i'} + \sum_{i=0}^{n_b-1} b_{0,i}^* b_{1,i} x_{01,0} + \left[\sum_{i'=1}^{n_b-1}\sum_{i=0}^{i'-1} b_{0,i} b_{1,i'}^* x_{10,i'-i}\right]^*. \tag{A.25}$$

The fourth term on the right-hand side of (A.1) is simplified using the same steps. Partitioning the inner summation for values of i' that produce positive, zero, and negative subscripts on x_{10} gives

$$\sum_{i=0}^{n_b-1}\sum_{i'=0}^{n_b-1} b_{1,i}^* b_{0,i'} x_{10,i-i'} = \sum_{i=0}^{n_b-1}\left[\sum_{i'=0}^{i-1} b_{1,i}^* b_{0,i'} x_{10,i-i'} + b_{1,i}^* b_{0,i} x_{10,0} + \sum_{i'=i+1}^{n_b-1} b_{1,i}^* b_{0,i'} x_{10,i-i'}\right] \tag{A.26}$$

$$= \sum_{i=1}^{n_b-1}\sum_{i'=0}^{i-1} b_{1,i}^* b_{0,i'} x_{10,i-i'} + \sum_{i=0}^{n_b-1} b_{1,i}^* b_{0,i} x_{10,0} + \sum_{i=0}^{n_b-2}\sum_{i'=0}^{i-1} b_{1,i}^* b_{0,i'} x_{10,i-i'}. \tag{A.27}$$

The second term on the right-hand side of (A.27) may be expressed as

$$\sum_{i=0}^{n_b-1} b_{1,i}^* b_{0,i} x_{10,0} = \sum_{i=0}^{n_b-1} b_{1,i}^* b_{0,i} x_{01,0}^* = \left[\sum_{i=0}^{n_b-1} b_{1,i} b_{0,i}^* x_{01,0}\right]^*. \tag{A.28}$$

The third term on the right-hand side of (A.27) is of the form (A.10). Exchanging the order of summation produces (cf. Figure A.1)

$$\sum_{i=0}^{n_b-2}\sum_{i'=0}^{i-1} b_{1,i}^* b_{0,i'} x_{10,i-i'} = \sum_{i'=1}^{n_b-1}\sum_{i=0}^{i'-1} b_{1,i}^* b_{0,i'} x_{10,i-i'} \tag{A.29}$$

$$= \sum_{i'=1}^{n_b-1}\sum_{i=0}^{i'-1} b_{1,i}^* b_{0,i'} x_{01,i'-i}^* \tag{A.30}$$

$$= \left[\sum_{i'=1}^{n_b-1}\sum_{i=0}^{i'-1} b_{1,i} b_{0,i'}^* x_{01,i'-i}\right]^*, \tag{A.31}$$

where the second step used the relationship (A.7). Substituting (A.31) in (A.27) produces

$$\sum_{i=0}^{n_b-1}\sum_{i'=0}^{n_b-1} b_{1,i}^* b_{0,i'} x_{10,i-i'}$$

$$= \sum_{i=1}^{n_b-1}\sum_{i'=0}^{i-1} b_{1,i}^* b_{0,i'} x_{10,i-i'} + \left[\sum_{i=0}^{n_b-1} b_{1,i} b_{0,i}^* x_{01,0}\right]^* + \left[\sum_{i'=1}^{n_b-1}\sum_{i=0}^{i'-1} b_{1,i} b_{0,i'}^* x_{01,i'-i}\right]^*. \tag{A.32}$$

Combining (A.25) and (A.32) gives

$$\sum_{i=0}^{n_b-1}\sum_{i'=0}^{n_b-1} b_{0,i}^* b_{1,i'} x_{01,i-i'} + \sum_{i=0}^{n_b-1}\sum_{i'=0}^{n_b-1} b_{1,i}^* b_{0,i'} x_{10,i-i'}$$

$$= 2\,\mathrm{Re}\left\{\sum_{i=1}^{n_b-1}\sum_{i'=0}^{i-1} b_{0,i}^* b_{1,i'} x_{01,i-i'} + \sum_{i=0}^{n_b-1} b_{0,i}^* b_{1,i} x_{01,0} + \sum_{i=1}^{n_b-1}\sum_{i'=0}^{i-1} b_{1,i}^* b_{0,i'} x_{10,i-i'}\right\}. \tag{A.33}$$

Two more steps are required to put (A.33) in the most useful form. First, using the substitution $m = i - i'$ in the first and third terms on the right-hand side of (A.33) produces

$$\sum_{i=0}^{n_b-1}\sum_{i'=0}^{n_b-1} b_{0,i}^* b_{1,i'} x_{01,i-i'} + \sum_{i=0}^{n_b-1}\sum_{i'=0}^{n_b-1} b_{1,i}^* b_{0,i'} x_{10,i-i'}$$

$$= 2\,\mathrm{Re}\left\{\sum_{i=1}^{n_b-1}\sum_{m=1}^{i} b_{0,i}^* b_{1,i-m} x_{01,m} + \sum_{i=0}^{n_b-1} b_{0,i}^* b_{1,i} x_{01,0} + \sum_{i=1}^{n_b-1}\sum_{m=1}^{i} b_{1,i}^* b_{0,i-m} x_{10,m}\right\}. \tag{A.34}$$

It is usually the case that $x_{01,m} = 0$ for $m > L_{01}$ for some integer $L_{01} \ll n_b$. Consequently, the upper limit on the inner summation of the first term on the right-hand side of (A.34) may be replaced by L_{01} if $b_{1,k} = 0$ for $k < 0$. Similarly, $x_{10,m} = 0$ for $m > L_{10}$ for some integer $L_{10} \ll n_b$ and the upper limit on the inner summation of the third term on the right-hand side of (A.34) may

be replaced by L_{10} if $b_{0,k} = 0$ for $k < 0$. Making these two changes gives

$$\sum_{i=0}^{n_b-1}\sum_{i'=0}^{n_b-1} b_{0,i}^* b_{1,i'} x_{01,i-i'} + \sum_{i=0}^{n_b-1}\sum_{i'=0}^{n_b-1} b_{1,i}^* b_{0,i'} x_{10,i-i'}$$
$$= 2\,\mathrm{Re}\left\{\sum_{i=1}^{n_b-1}\sum_{m=1}^{L_{01}} b_{0,i}^* b_{1,i-m} x_{01,m} + \sum_{i=0}^{n_b-1} b_{0,i}^* b_{1,i} x_{01,0} + \sum_{i=1}^{n_b-1}\sum_{m=1}^{L_{10}} b_{1,i}^* b_{0,i-m} x_{10,m}\right\}. \quad \text{(A.35)}$$

Next, we use the identity

$$2\,\mathrm{Re}\left\{\sum_{i=0}^{n_b-1} b_{0,i}^* b_{1,i} x_{01,0}\right\} = \mathrm{Re}\left\{\sum_{i=0}^{n_b-1} b_{0,i}^* b_{1,i} x_{01,0}\right\} + \mathrm{Re}\left\{\left[\sum_{i=0}^{n_b-1} b_{0,i}^* b_{1,i} x_{01,0}\right]^*\right\} \quad \text{(A.36)}$$
$$= \mathrm{Re}\left\{\sum_{i=0}^{n_b-1} b_{0,i}^* b_{1,i} x_{01,0}\right\} + \mathrm{Re}\left\{\sum_{i=0}^{n_b-1} b_{1,i}^* b_{0,i} x_{10,0}\right\}. \quad \text{(A.37)}$$

Substituting (A.37) and (A.35) into (A.33) gives

$$\sum_{i=0}^{n_b-1}\sum_{i'=0}^{n_b-1} b_{0,i}^* b_{1,i'} x_{01,i-i'} + \sum_{i=0}^{n_b-1}\sum_{i'=0}^{n_b-1} b_{1,i}^* b_{0,i'} x_{10,i-i'}$$
$$= \mathrm{Re}\left\{2\sum_{i=1}^{n_b-1}\sum_{m=1}^{L_{01}} b_{0,i}^* b_{1,i-m} x_{01,m} + \sum_{i=0}^{n_b-1} b_{0,i}^* b_{1,i} x_{01,0}\right\}$$
$$+ \mathrm{Re}\left\{2\sum_{i=1}^{n_b-1}\sum_{m=1}^{L_{10}} b_{1,i}^* b_{0,i-m} x_{10,m} + \sum_{i=0}^{n_b-1} b_{1,i}^* b_{0,i} x_{10,0}\right\}. \quad \text{(A.38)}$$

Substituting (A.16), (A.19), and (A.38) into (A.1) gives

$$\Lambda(\mathbf{I}) = \mathrm{Re}\left\{2\sum_{i=0}^{n_b-1} b_{0,i}^* y_{0,i} - 2\sum_{i=1}^{n_b-1}\sum_{m=-1}^{L_{00}} b_{0,i}^* b_{0,i-m} x_{00,m} - \sum_{i=0}^{n_b-1} b_{0,i}^* b_{0,i} x_{00,0}\right.$$
$$\left. -2\sum_{i=1}^{n_b-1}\sum_{m=1}^{L_{01}} b_{0,i}^* b_{1,i-m} x_{01,m} - \sum_{i=0}^{n_b-1} b_{0,i}^* b_{1,i} x_{01,0}\right\}$$
$$+ \mathrm{Re}\left\{2\sum_{i=0}^{n_b-1} b_{1,i}^* y_{1,i} - 2\sum_{i=1}^{n_b-1}\sum_{m=1}^{L_{11}} b_{1,i}^* b_{1,i-m} x_{11,m} - \sum_{i=0}^{n_b-1} b_{1,i}^* b_{1,i} x_{11,0}\right.$$
$$\left. -2\sum_{i=1}^{n_b-1}\sum_{i'=1}^{L_{10}} b_{1,i}^* b_{0,i-m} x_{10,m} - \sum_{i=0}^{n_b-1} b_{1,i}^* b_{0,i} x_{10,0}\right\}. \quad \text{(A.39)}$$

For notational reasons, it is convenient to define

$$L_x = \max\left\{L_{00}, L_{01}, L_{10}, L_{11}\right\} \tag{A.40}$$

and write

$$\begin{aligned}\Lambda(\mathbf{I}) = \text{Re}\Bigg\{ & 2\sum_{i=0}^{n_b-1} b_{0,i}^* y_{0,i} - 2\sum_{i=1}^{n_b-1}\sum_{m=1}^{L_x} b_{0,i}^* b_{0,i-m} x_{00,m} - \sum_{i=0}^{n_b-1} b_{0,i}^* b_{0,i} x_{00,0} \\ & -2\sum_{i=1}^{n_b-1}\sum_{m=1}^{L_x} b_{0,i}^* b_{1,i-m} x_{01,m} - \sum_{i=0}^{n_b-1} b_{0,i}^* b_{1,i} x_{01,0}\Bigg\} \\ + \text{Re}\Bigg\{ & 2\sum_{i=0}^{n_b-1} b_{1,i}^* y_{1,i} - 2\sum_{i=1}^{n_b-1}\sum_{m=1}^{L_x} b_{1,i}^* b_{1,i-m} x_{11,m} - \sum_{i=0}^{n_b-1} b_{1,i}^* b_{1,i} x_{11,0} \\ & -2\sum_{i=1}^{n_b-1}\sum_{i'=1}^{L_x} b_{1,i}^* b_{0,i-m} x_{10,m} - \sum_{i=0}^{n_b-1} b_{1,i}^* b_{0,i} x_{10,0}\Bigg\}. \end{aligned} \tag{A.41}$$

Factoring out the outer summation gives

$$\begin{aligned}\Lambda(\mathbf{I}) = & \text{Re}\left\{\sum_{i=0}^{n_b-1} b_{0,i}^*\left(2y_{0,i} - 2\sum_{m=-L_x}^{L_x} b_{0,i-m}x_{00,m} - b_{0,i}x_{00,0} - 2\sum_{m=-L_x}^{L_x} b_{1,i-m}x_{01,m} - b_{1,i}x_{01,0}\right)\right\} \\ & + \text{Re}\left\{\sum_{i=0}^{n_b-1} b_{1,i}^*\left(y_{1,i} - 2\sum_{m=-L_x}^{L_x} b_{1,i-m}x_{11,m} - b_{1,i}x_{11,0} - 2\sum_{i'=-L_x}^{L_x} b_{0,i-m}x_{10,m} - b_{0,i}x_{10,0}\right)\right\}. \end{aligned} \tag{A.42}$$

Note that lower limit of the summation with respect to i begins with $i = 0$ in (A.42) even though four of the summations with respect to i in (A.41) begin with $i = 1$. This change works as long as $b_{0,m} = b_{1,m} = 0$ for $m < 0$.

In preparation for use with the Viterbi Algorithm, (A.42) needs to be written in a recursive form. Let

$$\mathbf{I}_n = \begin{bmatrix} I_0 \\ \vdots \\ I_n \end{bmatrix} \tag{A.43}$$

for some $n \leq n_b$. Then

$$\Lambda(\mathbf{I}_n) = \text{Re}\left\{\sum_{i=0}^{n} b_{0,i}^*\left(2y_{0,i} - 2\sum_{m=1}^{L_x} b_{0,i-m}x_{00,m} - b_{0,i}x_{00,0} - 2\sum_{m=1}^{L_x} b_{1,i-m}x_{01,m} - b_{1,i}x_{01,0}\right)\right\}$$
$$+ \text{Re}\left\{\sum_{i=0}^{n} b_{1,i}^*\left(y_{1,i} - 2\sum_{m=1}^{L_x} b_{1,i'}x_{11,i-i'} - b_{1,i}x_{11,0} - 2\sum_{i'=1}^{L_x} b_{0,i-m}x_{10,m} - b_{0,i}x_{10,0}\right)\right\}$$
$$= \Lambda(\mathbf{I}_{n-1})$$
$$+ \text{Re}\left\{b_{0,n}^*\left(2y_{0,n} - 2\sum_{m=1}^{L_x} b_{0,n-m}x_{00,m} - b_{0,n}x_{00,0} - 2\sum_{m=1}^{L_x} b_{1,n-m}x_{01,m} - b_{1,n}x_{01,0}\right)\right\}$$
$$+ \text{Re}\left\{b_{1,n}^*\left(2y_{1,n} - 2\sum_{m=1}^{L_x} b_{1,n-m}x_{11,m} - b_{1,n}x_{11,0} - 2\sum_{i'=1}^{L_x} b_{0,n-m}x_{10,m} - b_{0,n}x_{10,0}\right)\right\}. \quad \text{(A.44)}$$

The partial path metric at time step $n-1$ corresponding to the sequence $\mathbf{I}_{n-1}$ is $\Lambda(\mathbf{I}_{n-1})$ and the partial path metric at time step n corresponding to the sequence $\mathbf{I}_n$ is $\Lambda(\mathbf{I}_n)$. The *branch metric* corresponding to $b_{0,n}$ and $b_{1,n}$ connected to the observations $y_{0,n}$ and $y_{1,n}$ is given by the second and third terms on the right-hand side of (A.44). After the pseudo-symbol substitutions from Equation (3.15), it is seen that the number of trellis states is

$$N_s = 2^{L_x+2}. \quad \text{(A.45)}$$

A.2 Equivalent Discrete-Time Model for the PAM Approximation

The log-likelihood function (A.42) operates on matched filter outputs $y_{0,i}$ and $y_{1,i}$ to find the maximum likelihood sequence as explained above. The outputs $y_{0,i}$ and $y_{1,i}$ form a discrete-time sequence for $0 \leq i < n_b$ corresponding to the input symbol sequence $\mathbf{I}$. This suggests an equivalent discrete-time system relating $\mathbf{I}$ to the sequence of outputs $y_{0,i}$ and $y_{1,i}$. The properties of this discrete-time system are derived from the expressions for $y_{0,i}$ and $y_{1,i}$.

The i-th matched filter output $y_{0,i}$ is

$$y_{0,i} = \int r_\ell(t)h_0^*(t - iT_b)dt \quad \text{(A.46)}$$
$$= \int \left[\sum_{k=0}^{n_b-1}\left\{b_{0,k}h_0(t - kT_b) + b_{1,k}h_1(t - kT_b)\right\} + z(t)\right] h_0^*(t - iT_b)dt \quad \text{(A.47)}$$

$$= \sum_{k=0}^{n_b-1} b_{0,k} \underbrace{\int h_0(t-kT_b)h_0^*(t-iT_b)dt}_{x_{00,i-k}} + \sum_{k=0}^{n_b-1} b_{1,k} \underbrace{\int h_1(t-kT_b)h_0^*(t-iT_b)dt}_{x_{01,i-k}}$$

$$+ \underbrace{\int z(t)h_0^*(t-iT_b)dt}_{\nu_{0,i}} \tag{A.48}$$

$$= \sum_{k=0}^{n_b-1} b_{0,k}x_{00,i-k} + \sum_{k=0}^{n_b-1} b_{1,k}x_{01,i-k} + \nu_{0,i}, \tag{A.49}$$

where the sequence $\nu_{0,i}$ is a complex-valued normal random sequence with zero mean and autocovariance

$$\mathrm{E}\left[\nu_{0,k}\nu_{0,\ell}^*\right] = \mathrm{E}\left[\int z(t)h_0^*(t-kT_b)dt \int z^*(t')h_0(t'-\ell T_b)dt'\right] \tag{A.50}$$

$$= \int\int \mathrm{E}\left[z(t)z^*(t')\right] h_0^*(t-kT_b)h_0(t'-\ell T_b)dt\,dt' \tag{A.51}$$

$$= \int\int 2N_0\delta(t-t')h_0^*(t-kT_b)h_0(t'-\ell T_b)dt\,dt' \tag{A.52}$$

$$= 2N_0 \int h_0^*(t'-kT_b)h_0(t'-\ell T_b)dt' \tag{A.53}$$

$$= 2N_0 x_{00,k-\ell}. \tag{A.54}$$

Similarly, the i-th matched filter output $y_{1,i}$ is

$$y_{1,i} = \int r_\ell(t)h_1^*(t-iT_b)dt \tag{A.55}$$

$$= \int \left[\sum_{k=0}^{n_b-1} \left\{b_{0,k}h_0(t-kT_b) + b_{1,k}h_1(t-kT_b)\right\} + z(t)\right] h_1^*(t-iT_b)dt \tag{A.56}$$

$$= \sum_{k=0}^{n_b-1} b_{0,k} \underbrace{\int h_0(t-kT_b)h_1^*(t-iT_b)dt}_{x_{10,i-k}} + \sum_{k=0}^{n_b-1} b_{1,k} \underbrace{\int h_1(t-kT_b)h_1^*(t-iT_b)dt}_{x_{11,i-k}}$$

$$+ \underbrace{\int z(t)h_1^*(t-iT_b)dt}_{\nu_{1,i}} \tag{A.57}$$

$$= \sum_{k=0}^{n_b-1} b_{0,k}x_{10,i-k} + \sum_{k=0}^{n_b-1} b_{1,k}x_{11,i-k} + \nu_{1,i}, \tag{A.58}$$

where the sequence $\nu_{1,i}$ is a complex-valued normal random sequence with zero mean and autocovariance

$$\mathrm{E}\left[\nu_{1,k}\nu_{1,\ell}^*\right] = \mathrm{E}\left[\int z(t)h_1^*(t-kT_b)dt \int z^*(t')h_1(t'-\ell T_b)dt'\right] \tag{A.59}$$

$$= \int\int \mathrm{E}\left[z(t)z^*(t')\right] h_1^*(t-kT_b)h_1(t'-\ell T_b)dt\,dt' \tag{A.60}$$

$$= \int\int 2N_0\delta(t-t')h_1^*(t-kT_b)h_1(t'-\ell T_b)dt\,dt' \tag{A.61}$$

$$= 2N_0\int h_1^*(t'-kT_b)h_1(t'-\ell T_b)dt' \tag{A.62}$$

$$= 2N_0 x_{11,k-\ell}. \tag{A.63}$$

The expressions (A.49) and (A.58) define the equivalent discrete-time system illustrated in Figure A.2. In the figure, the z-transforms are

$$X_{00}(z) = x_{00,-L_x}z^{L_x} + \cdots x_{00,0} + \cdots x_{00,L_x}z^{-L_x} \tag{A.64}$$

$$X_{01}(z) = x_{01,-L_x}z^{L_x} + \cdots x_{01,0} + \cdots x_{01,L_x}z^{-L_x} \tag{A.65}$$

$$X_{10}(z) = x_{10,-L_x}z^{L_x} + \cdots x_{10,0} + \cdots x_{10,L_x}z^{-L_x} \tag{A.66}$$

$$X_{11}(z) = x_{11,-L_x}z^{L_x} + \cdots x_{11,0} + \cdots x_{11,L_x}z^{-L_x}, \tag{A.67}$$

where L_x is defined in (A.40).

The relationships (A.49) and (A.58) may also be expressed in matrix-vector format. To do so, we define the following $n_b \times 1$ vectors

$$\mathbf{I} = \begin{bmatrix} I_0 \\ \vdots \\ I_{n_b-1} \end{bmatrix} \mathbf{b}_0 = \begin{bmatrix} b_{0,0} \\ \vdots \\ b_{0,n_b-1} \end{bmatrix} \mathbf{b}_1 = \begin{bmatrix} b_{1,0} \\ \vdots \\ b_{1,n_b-1} \end{bmatrix} \tag{A.68}$$

$$\mathbf{y}_0 = \begin{bmatrix} y_{0,0} \\ \vdots \\ y_{0,n_b-1} \end{bmatrix} \mathbf{y}_1 = \begin{bmatrix} y_{1,0} \\ \vdots \\ y_{1,n_b-1} \end{bmatrix} \boldsymbol{\nu}_0 = \begin{bmatrix} \nu_{0,0} \\ \vdots \\ \nu_{0,n_b-1} \end{bmatrix} \boldsymbol{\nu}_1 = \begin{bmatrix} \nu_{1,0} \\ \vdots \\ \nu_{1,n_b-1} \end{bmatrix}, \tag{A.69}$$

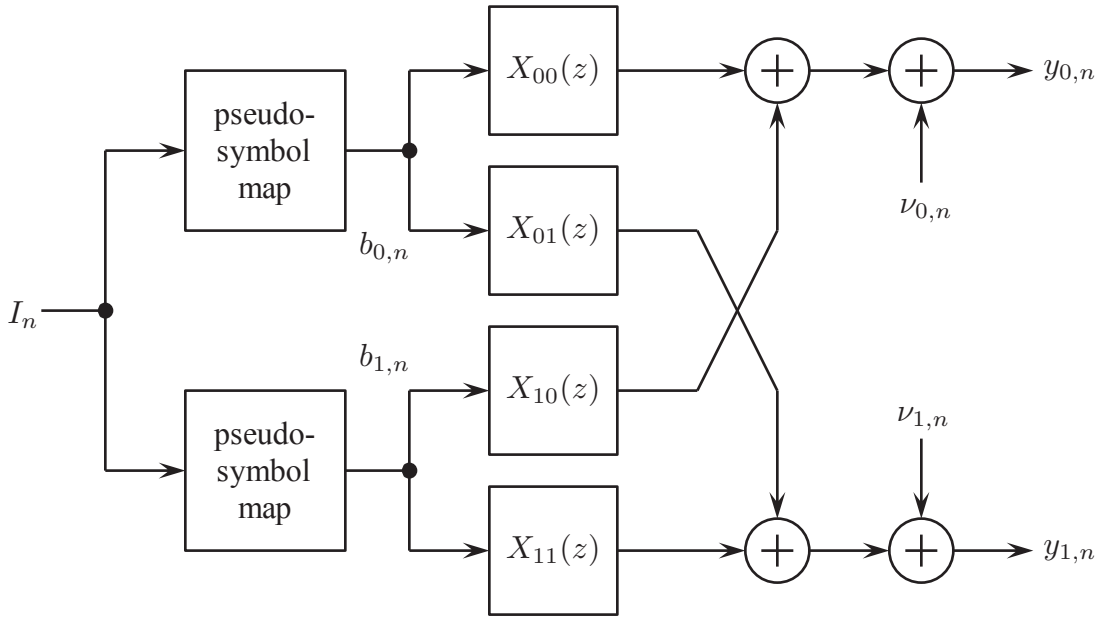

Figure A.2: A block diagram of the equivalent discrete-time system defined by Equations (A.49) and (A.58) for the PAM approximation.

and the following $n_b \times n_b$ convolution matrices

$$\mathbf{X}_{00} = \begin{bmatrix} x_{00,0} & x_{00,-1} & \cdots & x_{00,-L_x} & & \\ x_{00,1} & x_{00,0} & x_{00,-1} & \cdots & x_{00,-L_x} & \\ & & \ddots & & & \\ & & & \ddots & & \\ & & & & \ddots & \\ & & x_{00,L_x} & \cdots & x_{00,1} & x_{00,0} \end{bmatrix}. \tag{A.70}$$

$$\mathbf{X}_{01} = \begin{bmatrix} .x_{01,0} & x_{01,-1} & \cdots & x_{01,-L_x} & & \\ x_{01,1} & x_{01,0} & x_{01,-1} & \cdots & x_{01,-L_x} & \\ & & \ddots & & & \\ & & & \ddots & & \\ & & & & \ddots & \\ & & x_{01,L_x} & \cdots & x_{01,1} & x_{01,0} \end{bmatrix}. \tag{A.71}$$

$$\mathbf{X}_{10} = \begin{bmatrix} x_{10,0} & x_{10,-1} & \cdots & x_{10,-L_x} & & \\ x_{10,1} & x_{10,0} & x_{10,-1} & \cdots & x_{10,-L_x} & \\ & & \ddots & & & \\ & & & \ddots & & \\ & & & & \ddots & \\ & & x_{10,L_x} & \cdots & x_{10,1} & x_{10,0} \end{bmatrix}. \tag{A.72}$$

$$\mathbf{X}_{11} = \begin{bmatrix} x_{11,0} & x_{11,-1} & \cdots & x_{11,-L_x} & & \\ x_{11,1} & x_{11,0} & x_{11,-1} & \cdots & x_{11,-L_x} & \\ & & \ddots & & & \\ & & & \ddots & & \\ & & & & \ddots & \\ & & x_{11,L_x} & \cdots & x_{11,1} & x_{11,0} \end{bmatrix}. \tag{A.73}$$

Equipped with these definitions, the expressions (A.49) and (A.58) may be expressed as

$$\mathbf{y}_0 = \mathbf{X}_{00}\mathbf{b}_0 + \mathbf{X}_{01}\mathbf{b}_1 + \boldsymbol{\nu}_0 \tag{A.74}$$

$$\mathbf{y}_1 = \mathbf{X}_{10}\mathbf{b}_0 + \mathbf{X}_{11}\mathbf{b}_1 + \boldsymbol{\nu}_1. \tag{A.75}$$

Using (A.54) and (A.63), we see that

$$\boldsymbol{\nu}_0 \sim N(\mathbf{0}, 2N_0\mathbf{X}_{00}) \qquad \boldsymbol{\nu}_1 \sim N(\mathbf{0}, 2N_0\mathbf{X}_{11}). \tag{A.76}$$

Consequently,

$$\mathbf{y}_0 \mid \mathbf{I} \sim N\left(\mathbf{X}_{00}\mathbf{b}_0 + \mathbf{X}_{01}\mathbf{b}_1, 2N_0\mathbf{X}_{00}\right) \tag{A.77}$$

$$\mathbf{y}_1 \mid \mathbf{I} \sim N\left(\mathbf{X}_{10}\mathbf{b}_0 + \mathbf{X}_{11}\mathbf{b}_1, 2N_0\mathbf{X}_{11}\right). \tag{A.78}$$

It should be noted that the vectors $\mathbf{y}_0$ and $\mathbf{y}_1$ are not statistically independent. This is for two reasons: first both $\mathbf{y}_0$ and $\mathbf{y}_1$ are a function of the common data sequence $\mathbf{I}$. Second, the noise sequences $\nu_{0,i}$ and $\nu_{1,i}$ are not uncorrelated. That this is true follows from the fact that the covariance is not zero:

$$\mathrm{E}\left[\nu_{0,k}\nu_{1,\ell}^*\right] = \mathrm{E}\left[\int z(t)h_0^*(t-kT_b)dt \int z^*(t')h_1(t'-\ell T_b)dt'\right] \tag{A.79}$$

$$= \int\int \mathrm{E}\left[z(t)z^*(t')\right] h_0^*(t-kT_b)h_1(t'-\ell T_b)dt\,dt' \tag{A.80}$$

$$= \int\int 2N_0\delta(t-t')h_0^*(t-kT_b)h_1(t'-\ell T_b)dt\,dt' \tag{A.81}$$

$$= 2N_0 \int h_0^*(t'-kT_b)h_1(t'-\ell T_b)dt' \tag{A.82}$$

$$= 2N_0 x_{01,k-\ell}. \tag{A.83}$$

A.3 Analysis of the Equivalent Discrete-Time Model: Insight Into the Structure of the Maximum Likelihood Equalizer

The maximum likelihood equalizer derives from the joint distribution of $\mathbf{y}_0$ and $\mathbf{y}_1$. To derive the joint distribution, we first note that the sequences $\nu_{0,i}$ and $\nu_{1,i}$ are jointly normal complex-valued random sequences with zero mean and cross-covariance given by (A.83). Consequently, the vectors $\boldsymbol{\nu}_0$ and $\boldsymbol{\nu}_1$ are distributed as

$$\begin{bmatrix}\boldsymbol{\nu}_0\\ \boldsymbol{\nu}_1\end{bmatrix} \sim N\left(\begin{bmatrix}\mathbf{0}\\ \mathbf{0}\end{bmatrix}, 2N_0\begin{bmatrix}\mathbf{X}_{00} & \mathbf{X}_{01}\\ \mathbf{X}_{10} & \mathbf{X}_{11}\end{bmatrix}\right). \tag{A.84}$$

Conditionally, $\mathbf{y}_0$ and $\mathbf{y}_1$ are jointly distributed as

$$\begin{bmatrix}\mathbf{y}_0\\ \mathbf{y}_1\end{bmatrix} \mid \mathbf{I} \sim N\left(\begin{bmatrix}\mathbf{X}_{00} & \mathbf{X}_{01}\\ \mathbf{X}_{10} & \mathbf{X}_{11}\end{bmatrix}\begin{bmatrix}\mathbf{b}_0\\ \mathbf{b}_1\end{bmatrix}, 2N_0\begin{bmatrix}\mathbf{X}_{00} & \mathbf{X}_{01}\\ \mathbf{X}_{10} & \mathbf{X}_{11}\end{bmatrix}\right). \tag{A.85}$$

To compute the log-likelihood function, we use the notation

$$\mathbf{y} = \begin{bmatrix}\mathbf{y}_0\\ \mathbf{y}_1\end{bmatrix} \mathbf{b} = \begin{bmatrix}\mathbf{b}_0\\ \mathbf{b}_1\end{bmatrix} \mathbf{X} = \begin{bmatrix}\mathbf{X}_{00} & \mathbf{X}_{01}\\ \mathbf{X}_{10} & \mathbf{X}_{11}\end{bmatrix} \tag{A.86}$$

so that the conditional density of $\mathbf{y}$ may be expressed as

$$p(\mathbf{y} \mid \mathbf{I}) = \frac{1}{(2\pi N_0)^{2n_b}\,|\mathbf{X}|} \exp\left\{-(\mathbf{y}-\mathbf{X}\mathbf{b})^\dagger (2N_0\mathbf{X})^{-1}(\mathbf{y}-\mathbf{X}\mathbf{b})\right\}. \tag{A.87}$$

From this, the log-likelihood function is seen to be

$$\Lambda(\mathbf{I}) = -\ln\left\{ (2\pi N_0)^{2n_b} |\mathbf{X}| \right\} - \frac{1}{2N_0} (\mathbf{y} - \mathbf{X}\mathbf{b})^\dagger \mathbf{X}^{-1} (\mathbf{y} - \mathbf{X}\mathbf{b}) . \tag{A.88}$$

Discarding terms that have no functional dependence on $\mathbf{I}$, the we may use, as the log-likelihood function

$$\Lambda(\mathbf{I}) = \mathbf{y}^\dagger \mathbf{X}^{-1} \mathbf{X}\mathbf{b} + \mathbf{b}^\dagger \mathbf{X}^\dagger \mathbf{X}^{-1} \mathbf{y} - \mathbf{b}^\dagger \mathbf{X}^\dagger \mathbf{X}^{-1} \mathbf{X}\mathbf{b} \tag{A.89}$$

$$= \mathbf{y}^\dagger \mathbf{b} + \mathbf{b}^\dagger \mathbf{y} - \mathbf{b}^\dagger \mathbf{X}\mathbf{b} \tag{A.90}$$

$$= 2\,\mathrm{Re}\left\{ \mathbf{b}^\dagger \mathbf{y} \right\} - \mathbf{b}^\dagger \mathbf{X}\mathbf{b}, \tag{A.91}$$

where the second step relies on the fact that $\mathbf{X}$ is Hermitian ($\mathbf{X}^\dagger = \mathbf{X}$). Using the substitutions (A.86), the log-likelihood function may be expressed as

$$\Lambda(\mathbf{I}) = 2\,\mathrm{Re}\left\{ \mathbf{b}_0^\dagger \mathbf{y}_0 + \mathbf{b}_1^\dagger \mathbf{y}_1 \right\} - \mathbf{b}_0^\dagger \mathbf{X}_{00} \mathbf{b}_0 - \mathbf{b}_0^\dagger \mathbf{X}_{01} \mathbf{b}_1 - \mathbf{b}_1^\dagger \mathbf{X}_{10} \mathbf{b}_0 - \mathbf{b}_1^\dagger \mathbf{X}_{11} \mathbf{b}_1 . \tag{A.92}$$

Now, to create the recursion necessary to formulate the Viterbi Algorithm, the inner products of (A.92) need to written as double-summations where the upper limit of the upper limit of the index for the inner summation does not exceed the index of the outer summation. To see how this works, consider the following $N \times 1$ vectors and the $N \times N$ matrix

$$\mathbf{u} = \begin{bmatrix} u_0 \\ \vdots \\ u_{N-1} \end{bmatrix} \quad \mathbf{v} = \begin{bmatrix} v_0 \\ \vdots \\ v_{N-1} \end{bmatrix} \quad \mathbf{M} = \begin{bmatrix} m_{0,0} & m_{0,1} & \cdots & m_{0,N-1} \\ m_{1,0} & m_{1,1} & \cdots & m_{1,N-1} \\ \vdots & & & \\ m_{N-1,0} & m_{N-1,1} & \cdots & m_{N-1,N-1} \end{bmatrix} . \tag{A.93}$$

The inner product $\mathbf{u}^\dagger \mathbf{M} \mathbf{v}$ may be expressed as

$$\mathbf{u}^\dagger \mathbf{M} \mathbf{v} = \sum_{k=0}^{N-1} \sum_{\ell=0}^{N-1} u_k^* m_{k,\ell} v_\ell . \tag{A.94}$$

Expressions of this form cannot be used in the Viterbi Algorithm because a recursion cannot be constructed. But if the upper limit of the inner summation could be restricted to a value no greater

than k, then a recursion could be constructed. To see how this might manifest itself with matrix/vector notation, consider writing $\mathbf{M}$ as the sum of a lower triangular portion of $\mathbf{M}$, the diagonal elements of $\mathbf{M}$, and the upper triangular portion of $\mathbf{M}$:

$$\mathbf{M} = \mathbf{M}_L + \mathbf{M}_D + \mathbf{M}_U, \tag{A.95}$$

where

$$\mathbf{M}_L = \begin{bmatrix} 0 & 0 & \cdots & 0 \\ m_{1,0} & 0 & \cdots & 0 \\ \vdots & & \ddots & \vdots \\ m_{N-1,0} & \cdots & m_{N-1,N-2} & 0 \end{bmatrix} \tag{A.96}$$

$$\mathbf{M}_D = \begin{bmatrix} m_{0,0} & 0 & \cdots & 0 \\ 0 & m_{1,1} & \cdots & 0 \\ \vdots & & \ddots & \\ 0 & \cdots & 0 & m_{N-1,N-1} \end{bmatrix} \tag{A.97}$$

$$\mathbf{M}_U = \begin{bmatrix} 0 & m_{0,1} & \cdots & m_{0,L-1} \\ 0 & 0 & \cdots & m_{1,L-1} \\ \vdots & \vdots & \ddots & \\ 0 & 0 & \cdots & 0 \end{bmatrix} \tag{A.98}$$

Now we may write

$$\mathbf{u}^\dagger \mathbf{M} \mathbf{v} = \mathbf{u}^\dagger \mathbf{M}_L \mathbf{v} + \mathbf{u}^\dagger \mathbf{M}_D \mathbf{v} + \mathbf{u}^\dagger \mathbf{M}_U \mathbf{v} \tag{A.99}$$

or, in terms of the double summations,

$$\mathbf{u}^\dagger \mathbf{M} \mathbf{v} = \underbrace{\sum_{k=0}^{L-1} \sum_{\ell=0}^{k-1} u_k^* m_{k,\ell} v_\ell}_{\mathbf{u}^\dagger \mathbf{M}_L \mathbf{v}} + \underbrace{\sum_{k=0}^{L-1} u_k^* m_{k,k} v_k}_{\mathbf{u}^\dagger \mathbf{M}_D \mathbf{v}} + \underbrace{\sum_{k=0}^{L-1} \sum_{\ell=k+1}^{L-1} u_k^* m_{k,\ell} v_\ell}_{\mathbf{u}^\dagger \mathbf{M}_U \mathbf{v}}. \tag{A.100}$$

The first two terms on the right-hand side of (A.100) work with the Viterbi algorithm. Unfortunately, the last term on the right-hand side of (A.100) does not work with the Viterbi algorithm. Thus, in general, expressing the square matrix involved in a quadratic equation of the form (A.94)

in terms of its lower triangular, diagonal, and upper triangular submatrices does not produce an expression compatible with the Viterbi Algorithm. But in the case under consideration, the symmetries of the auto- and cross-correlation matrices are such that a Viterbi-Algorithm-compatible form is possible.

The goal then is to express each of the quadratic forms in (A.92) in terms of lower triangular and diagonal matrices. The starting point is the second term on the right-hand side of (A.92). Expressing $\mathbf{X}_{00}$ as $\mathbf{X}_{00,L} + \mathbf{X}_{00,D} + \mathbf{X}_{00,U}$ gives

$$\begin{aligned}
\mathbf{b}_0^\dagger \mathbf{X}_{00} \mathbf{b}_0 &= \mathbf{b}_0^\dagger \mathbf{X}_{00,L} \mathbf{b}_0 + \mathbf{b}_0^\dagger \mathbf{X}_{00,D} \mathbf{b}_0 + \mathbf{b}_0^\dagger \mathbf{X}_{00,U} \mathbf{b}_0 && \text{(A.101)} \\
&= \mathbf{b}_0^\dagger \mathbf{X}_{00,L} \mathbf{b}_0 + \mathbf{b}_0^\dagger \mathbf{X}_{00,D} \mathbf{b}_0 + \mathbf{b}_0^\dagger \mathbf{X}_{00,L}^\dagger \mathbf{b}_0 && \text{(A.102)} \\
&= \mathbf{b}_0^\dagger \mathbf{X}_{00,L} \mathbf{b}_0 + \mathbf{b}_0^\dagger \mathbf{X}_{00,D} \mathbf{b}_0 + \left(\mathbf{b}_0^\dagger \mathbf{X}_{00,L} \mathbf{b}_0 \right)^\dagger && \text{(A.103)} \\
&= 2\,\mathrm{Re}\left[\mathbf{b}_0^\dagger \mathbf{X}_{00,L} \mathbf{b}_0 \right] + \mathbf{b}_0^\dagger \mathbf{X}_{00,D} \mathbf{b}_0, && \text{(A.104)}
\end{aligned}$$

where the second step follows from the conjugate symmetry $x_{00}(-m) = x_{00}^*(m)$. Similarly, the fifth term on the right-hand side of (A.92) may be expressed as

$$\mathbf{b}_1^\dagger \mathbf{X}_{11} \mathbf{b}_1 = 2\,\mathrm{Re}\left[\mathbf{b}_1^\dagger \mathbf{X}_{11,L} \mathbf{b}_1 \right] + \mathbf{b}_1^\dagger \mathbf{X}_{11,D} \mathbf{b}_1, \tag{A.105}$$

which follows from the conjugate symmetry $x_{11}(-m) = x_{11}^*(m)$.

For the third and fourth terms of (A.92), the symmetries are different [cf. (A.7)], so these two terms need to be considered together:

$$\begin{aligned}
&\mathbf{b}_0^\dagger \mathbf{X}_{01} \mathbf{b}_1 + \mathbf{b}_1^\dagger \mathbf{X}_{10} \mathbf{b}_0 \\
&\quad = \mathbf{b}_0^\dagger \left(\mathbf{X}_{01,L} + \mathbf{X}_{01,D} + \mathbf{X}_{01,U} \right) \mathbf{b}_1 + \mathbf{b}_1^\dagger \left(\mathbf{X}_{10,L} + \mathbf{X}_{10,D} + \mathbf{X}_{10,U} \right) \mathbf{b}_0 && \text{(A.106)} \\
&\quad = \mathbf{b}_0^\dagger \left(\mathbf{X}_{01,L} + \mathbf{X}_{01,D} + \mathbf{X}_{10,L}^\dagger \right) \mathbf{b}_1 + \mathbf{b}_1^\dagger \left(\mathbf{X}_{10,L} + \mathbf{X}_{10,D} + \mathbf{X}_{01,L}^\dagger \right) \mathbf{b}_0 && \text{(A.107)} \\
&\quad = \underbrace{\mathbf{b}_0^\dagger \mathbf{X}_{01,L} \mathbf{b}_1 + \mathbf{b}_1^\dagger \mathbf{X}_{01,L}^\dagger \mathbf{b}_0}_{2\,\mathrm{Re}\left[\mathbf{b}_0^\dagger \mathbf{X}_{01,L} \mathbf{b}_1 \right]} + \underbrace{\mathbf{b}_0^\dagger \mathbf{X}_{10,L}^\dagger \mathbf{b}_1 + \mathbf{b}_1^\dagger \mathbf{X}_{10,L} \mathbf{b}_0}_{2\,\mathrm{Re}\left[\mathbf{b}_1^\dagger \mathbf{X}_{10,L} \mathbf{b}_0 \right]} + \underbrace{\mathbf{b}_0^\dagger \mathbf{X}_{01,D} \mathbf{b}_1 + \mathbf{b}_1^\dagger \mathbf{X}_{10,D} \mathbf{b}_0}_{2\,\mathrm{Re}\left[\mathbf{b}_0^\dagger \mathbf{X}_{01,D} \mathbf{b}_1 \right]}. && \text{(A.108)}
\end{aligned}$$

Because the third term on the right-hand side of (A.108) may be written as

$$2\,\mathrm{Re}\left[\mathbf{b}_0^\dagger \mathbf{X}_{01,D}\mathbf{b}_1\right] = \mathrm{Re}\left[\mathbf{b}_0^\dagger \mathbf{X}_{01,D}\mathbf{b}_1\right] + \mathrm{Re}\left[\mathbf{b}_1^\dagger \mathbf{X}_{10,D}\mathbf{b}_0\right], \tag{A.109}$$

$\mathbf{b}_0^\dagger \mathbf{X}_{01}\mathbf{b}_1 + \mathbf{b}_1^\dagger \mathbf{X}_{10}\mathbf{b}_0$ may be expressed in the slightly more useful form

$$\begin{aligned}\mathbf{b}_0^\dagger \mathbf{X}_{01}\mathbf{b}_1 + \mathbf{b}_1^\dagger \mathbf{X}_{10}\mathbf{b}_0 = \\ 2\,\mathrm{Re}\left[\mathbf{b}_0^\dagger \mathbf{X}_{01,L}\mathbf{b}_1\right] + \mathrm{Re}\left[\mathbf{b}_0^\dagger \mathbf{X}_{01,D}\mathbf{b}_1\right] + 2\,\mathrm{Re}\left[\mathbf{b}_1^\dagger \mathbf{X}_{10,L}\mathbf{b}_0\right] + \mathrm{Re}\left[\mathbf{b}_1^\dagger \mathbf{X}_{10,D}\mathbf{b}_0\right].\end{aligned} \tag{A.110}$$

Substituting (A.104), (A.105), and (A.110) into (A.92) gives

$$\begin{aligned}\Lambda(\mathbf{I}) &= 2\,\mathrm{Re}\left\{\mathbf{b}_0^\dagger \mathbf{y}_0\right\} - 2\,\mathrm{Re}\left[\mathbf{b}_0^\dagger \mathbf{X}_{00,L}\mathbf{b}_0\right] - \mathbf{b}_0^\dagger \mathbf{X}_{00,D}\mathbf{b}_0 - 2\,\mathrm{Re}\left[\mathbf{b}_0^\dagger \mathbf{X}_{01,L}\mathbf{b}_1\right] - \mathrm{Re}\left[\mathbf{b}_0^\dagger \mathbf{X}_{01,D}\mathbf{b}_1\right] \\ &\quad + 2\,\mathrm{Re}\left\{\mathbf{b}_1^\dagger \mathbf{y}_1\right\} - 2\,\mathrm{Re}\left[\mathbf{b}_1^\dagger \mathbf{X}_{11,L}\mathbf{b}_1\right] - \mathbf{b}_1^\dagger \mathbf{X}_{11,D}\mathbf{b}_1 - 2\,\mathrm{Re}\left[\mathbf{b}_1^\dagger \mathbf{X}_{10,L}\mathbf{b}_0\right] - \mathrm{Re}\left[\mathbf{b}_1^\dagger \mathbf{X}_{10,D}\mathbf{b}_0\right]. \\ &= \mathrm{Re}\left[2\mathbf{b}_0^\dagger \mathbf{y}_0 - 2\mathbf{b}_0^\dagger \mathbf{X}_{00,L}\mathbf{b}_0 - \mathbf{b}_0^\dagger \mathbf{X}_{00,D}\mathbf{b}_0 - 2\mathbf{b}_0^\dagger \mathbf{X}_{01,L}\mathbf{b}_1 - \mathbf{b}_0^\dagger \mathbf{X}_{01,D}\mathbf{b}_1\right] \\ &\quad + \mathrm{Re}\left[2\mathbf{b}_1^\dagger \mathbf{y}_1 - 2\mathbf{b}_1^\dagger \mathbf{X}_{11,L}\mathbf{b}_1 - \mathbf{b}_1^\dagger \mathbf{X}_{11,D}\mathbf{b}_1 - 2\mathbf{b}_1^\dagger \mathbf{X}_{10,L}\mathbf{b}_0 - \mathbf{b}_1^\dagger \mathbf{X}_{10,D}\mathbf{b}_0\right] \\ &= \mathrm{Re}\left[\mathbf{b}_0^\dagger \left(2\mathbf{y}_0 - 2\mathbf{X}_{00,L}\mathbf{b}_0 - \mathbf{X}_{00,D}\mathbf{b}_0 - 2\mathbf{X}_{01,L}\mathbf{b}_1 - \mathbf{X}_{01,D}\mathbf{b}_1\right)\right] \\ &\quad + \mathrm{Re}\left[\mathbf{b}_1^\dagger \left(2\mathbf{y}_1 - 2\,\mathbf{X}_{11,L}\mathbf{b}_1 - \mathbf{X}_{11,D}\mathbf{b}_1 - 2\mathbf{X}_{10,L}\mathbf{b}_0 - \mathbf{X}_{10,D}\mathbf{b}_0\right)\right].\end{aligned} \tag{A.111}$$

Writing out the vector/matrix products as sums gives

$$\begin{aligned}\Lambda(\mathbf{I}) &= \mathrm{Re}\left[\sum_{i=0}^{n_b-1} b_{0,i}^* \left(2y_{0,i} - 2\sum_{i'=0}^{i-1} x_{00,i-i'}b_{0,i'} - x_{00,0}b_{0,i} - 2\sum_{i'=0}^{i-1} x_{01,i}b_{1,i'} - x_{01,0}b_{1,i}\right)\right] \\ &+ \mathrm{Re}\left[\sum_{i=0}^{n_b-1} b_{1,i}^* \left(2y_{1,i} - 2\sum_{i'=0}^{i-1} x_{11,i-i'}b_{1,i'} - x_{11,0}b_{1,i} - 2\sum_{i'=0}^{i-1} x_{10,i-i'}b_{0,i'} - x_{10,0}b_{0,i}\right)\right].\end{aligned} \tag{A.112}$$

Using the substitution $m = i - i'$ gives

$$\begin{aligned}\Lambda(\mathbf{I}) &= \mathrm{Re}\left[\sum_{i=0}^{n_b-1} b_{0,i}^* \left(2y_{0,i} - 2\sum_{m=1}^{i} x_{00,m}b_{0,i-m} - x_{00,0}b_{0,i} - 2\sum_{m=1}^{i} x_{01,m}b_{1,i-m} - x_{01,0}b_{1,i}\right)\right] \\ &\quad + \mathrm{Re}\left[\sum_{i=0}^{n_b-1} b_{1,i}^* \left(2y_{1,i} - 2\sum_{m=1}^{i} x_{11,m}b_{1,i-m} - x_{11,0}b_{1,i} - 2\sum_{m=1}^{i-1} x_{10,m}b_{0,i-m} - x_{10,0}b_{0,i}\right)\right].\end{aligned} \tag{A.113}$$

Finally, using (A.40) and the discussion surrounding (A.40) regarding the support for the auto- and cross-correlations, we obtain

$$\Lambda(\mathbf{I}) = \mathrm{Re}\left[\sum_{i=0}^{n_b-1} b_{0,i}^* \left(2y_{0,i} - 2\sum_{m=1}^{L_x} x_{00,m} b_{0,i-m} - x_{00,0} b_{0,i} - 2\sum_{m=1}^{L_x} x_{01,m} b_{1,i-m} - x_{01,0} b_{1,i}\right)\right] + \mathrm{Re}\left[\sum_{i=0}^{n_b-1} b_{1,i}^* \left(2y_{1,i} - 2\sum_{m=1}^{L_x} x_{11,m} b_{1,i-m} - x_{11,0} b_{1,i} - 2\sum_{m=1}^{i-1} x_{10,m} b_{0,i-m} - x_{10,0} b_{0,L_x}\right)\right]. \tag{A.114}$$

The log-likelihood function (A.114) is identical to the log-likelihood function (A.42). The point here is that the terms involving $x_{00,\cdot}$, $x_{01,\cdot}$, $x_{10,\cdot}$, and $x_{11,\cdot}$ are needed to account for the noise correlation in the branch-metric computations.